

CRANFIELD UNIVERSITY

Aitzol Onaindia

BAE JETSTREAM 31 UNDERCARRIAGE DRAG ANALYSIS

School of Aerospace, Transport and Manufacturing
Aerospace Dynamics

MSc
Academic Year: 2018 - 2019

Supervisor: Prof. Nicholas J. Lawson
Associate Supervisor: Dr Christopher J. Bennett
August 2019

CRANFIELD UNIVERSITY

School of Aerospace, Transport and Manufacturing
Aerospace Dynamics

MSc

Academic Year 2018 - 2019

Aitzol Onaindia

BAE JETSTREAM 31 UNDERCARRIAGE DRAG ANALYSIS

Supervisor: Prof. Nicholas J. Lawson
Associate Supervisor: Dr Christopher J. Bennett
August 2019

This thesis is submitted in partial fulfilment of the requirements for
the degree of MSc in Aerospace Dynamics
***(NB. This section can be removed if the award of the degree is
based solely on examination of the thesis)***

© Cranfield University 2019. All rights reserved. No part of this
publication may be reproduced without the written permission of the
copyright owner.

ABSTRACT

The following report presents the undercarriage drag predictions for the retractable landing gear of the BAE Jetstream 31, operated by the National Flying Laboratory Centre (NFLC) at Cranfield University. A model of the landing gear was incorporated to the laser scanned model of the aircraft, and Computational Fluid Dynamics (CFD) techniques were used to measure the undercarriage drag. These results are compared to the flight experiments and empirical methods, and the CFD drag predictions are just below the prediction intervals for small angles of attack. Due to the flow field and lack of the propellers more discrepancies are observed in lift and drag at higher angles of attack.

Keywords:

CFD, retractable landing gear, lift coefficient, turbulence, cylinder flow, cavity flow, ESDU, NFLC

ACKNOWLEDGEMENTS

I would like to thank my supervisor Prof. Nicholas Lawson and Dr Chris Bennet (NFLC) for the support and guidance during the project. Their experience in the area has been very helpful, particularly when it comes to the analysis of the results.

I would also like to thank Dr Alastair Cooke for the data provided from the flight tests which was necessary for the validation of the methods tested.

CONTENTS

ABSTRACT	i
ACKNOWLEDGEMENTS	ii
LIST OF FIGURES	v
LIST OF TABLES	vi
1 INTRODUCTION	1
1.1 Aims	2
1.2 Objectives	2
2 LITERATURE REVIEW	3
2.1 Undercarriage drag sources	3
2.1.1 Flow across cylinders	3
2.1.2 Drag of flat plates.....	6
2.1.3 Cavity flow	7
2.2 Drag prediction techniques.....	9
2.2.1 Empirical methods	9
2.2.2 Computational methods.....	9
2.2.3 Experimental methods	9
2.3 Mesh generation	10
2.3.1 Mesh types	10
2.3.2 Mesh quality.....	11
2.4 CFD of an aircraft with the undercarriage.....	12
2.4.1 Governing equations.....	12
2.4.2 Turbulence models	13
2.5 Previous investigation with the Jetstream	15
2.6 Other areas of interest. Aeroacoustics	15
3 METHODOLOGY	16
3.1 Computer-aided design (CAD)	16
3.2 Mesh generation	18
3.3 Computational fluid dynamics (CFD).....	19
3.3.1 Solver	19
3.3.2 Post processor.....	20
3.3.3 Mesh dependency study.....	20
3.3.4 Turbulence model study	21
3.4 Validation of results.....	22
4 UNDECARRIAGE DRAG ANALYSIS	23
4.1 CFD model	23
4.1.1 Cruise configuration.....	23
4.1.2 UCDWN configuration	25
4.2 ESDU method	30
4.2.1 Front gear drag.....	31
4.2.2 Main gear drag.....	38
5 CONCLUSIONS AND FURTHER RECOMMENDATIONS	43
5.1 Conclusions.....	43
5.2 Future work	44

6	REFERENCES.....	45
Appendix A.	PARAMETERS OF THE MESH.....	48
Appendix B.	FLUENT SETTINGS	52
Appendix C.	DRAG COEFFICIENT OF EACH ELEMENT.....	56
Appendix D.	FLOW VISUALIZATION	57
Appendix E.	FLOW STRUCTURE IN EACH COMPONENT.....	60

LIST OF FIGURES

Figure 2.1.1. Flow separation mechanism on a cylinder for different Reynolds number [4]	4
Figure 2.1.2. Drag coefficient of a cylinder as a function of Reynolds number [5]	6
Figure 2.1.3. Drag coefficient of a flat plate [5]	7
Figure 2.1.4. Closed and open cavity flows [10]	8
Figure 3.1.1. Front gear CAD model	17
Figure 3.1.2. Main gear CAD model	18
Figure 4.1.1. Lift characteristics at CR configuration	23
Figure 4.1.2. Drag polar at CR configuration	24
Figure 4.1.3. Lift characteristics at UCDWN configuration	25
Figure 4.1.4. Spanwise vertical force coefficient comparison	26
Figure 4.1.5. Pressure contours of the wing at CR and UCDWN configurations, where the arrow shows the freestream flow direction. ($M=0.25$, $\alpha=2^\circ$)	27
Figure 4.1.6. Flow visualisation of the lower surface of the wing, where the arrow indicates the direction of the freestream flow. ($M=0.25$, $\alpha=2^\circ$)	28
Figure 4.1.7. Drag polar at UCDWN configuration	28
Figure 4.2.1. Dimensions of the front gear (in mm)	31
Figure 4.2.2. Front gear drag estimates, ESDU and CFD.	35
Figure 4.2.3. Flow past the nose of the aircraft at CR and UCDWN respectively, $M=0.25$ $\alpha=7^\circ$	36
Figure 4.2.4. Pressure contours for CR and UCDWN configurations, $M=0.25$ $\alpha=7^\circ$	37
Figure 4.2.5. Dimensions of the main gear (in mm)	38
Figure 4.2.6. Drag coefficient of each main gear mechanism	40
Figure 4.2.7. Flow past the main gear, $M=0.25$ $\alpha=7^\circ$. (Horizontal lines plotted to visualize the change in angle of the streamlines)	41
Figure 4.2.8. Total drag, comparison of different methods	41

LIST OF TABLES

Table 3.3.1. Lift and drag variations with different mesh densities	21
Table 3.3.2. Lift and drag variations with different turbulence models.....	22

1 INTRODUCTION

In this report I present a computational fluid dynamics (CFD) study of the undercarriage of the Cranfield University Jetstream 31. The Jetstream is the airplane of the National Flying Laboratory Centre (NFLC) and is being used as a flying engineering laboratory by over 25 universities [1]. Flight test data from over 15 years is currently available, therefore making the aircraft an ideal choice for the study of different computational models regarding different aspects of the plane, in this case the area of interest is the effect of landing gear on a full CFD model of the aircraft.

The aircraft is powered by two co-rotating turbo-prop engines, with a maximum take-off weight of 7059 kg. It was modified to convert it into a flying laboratory allowing a maximum of 18 passengers.

The aircraft is equipped with numerous sensors, in addition to the pitot-static system which provides air data needed to pilot as the airspeed and altitude, to facilitate its role as a flying laboratory. The instrumentation contains:

- force sensors in the elevator and rudder circuits;
- position sensors on the flaps, aileron, rudder, elevator and elevator trim tab;
- an engine signal interface;
- a video camera;
- an inertial reference system (IRS) located and controlled from the rear of the cabin;
- an air data computer (ADC);
- a NAV and DME receiver: controllable from the rear of the cabin (additional to standard fit of two controlled from the cockpit);
- a GPS receiver;
- a differential pressure gauge that compares S6 with S2;
- angle of attack and sideslip vanes.

The data needed in this project was the airspeed, angle of attack, weight of the aircraft in each flight and the power generated by the engine. Other useful

information was the altitude or ambient pressure of the tests to set up the computational cases.

1.1 Aims

The aim of the project is to validate a CFD model of the Jetstream 31 aircraft with undercarriage with flight test data obtained from steady, level flight tests and other drag prediction methods, including ESDU and theoretical methods.

Once the main goal was reached, some drag reduction techniques were intended to find from previous studies and the literature suitable for the case analysed.

1.2 Objectives

The aims are going to be achieved following the objectives defined in the following paragraph. For the first part of the project the objectives are:

- Modify an existing model of the Jetstream to incorporate the undercarriage components.
- Generate a mesh that can predict the drag as accurately as possible with a reasonable computational cost by doing a mesh sensitivity analysis.
- Obtain reliable steady state data comparing the results of the computational model and flight test data.
- Compare different drag prediction methods (CFD, flight tests and theoretical methods) analysing the errors, advantages, disadvantages and possible sources of the discrepancies.

2 LITERATURE REVIEW

The effect of the retractable undercarriage drag during the design process is important as it will increment the drag during the take-off while the maximum thrust from the engines is needed [2]. During the approach and landing the handling and performance characteristics of the aircraft will be influenced by the change in the configuration. A sudden increase in drag and nose down pitching moment due to the application point of the incremental drag, below the centre of gravity, will appear while the aircraft is flying near the ground.

These characteristics of the retractable landing gear makes the prediction of the undercarriage drag an area of interest.

2.1 Undercarriage drag sources

A retractable landing gear is formed by wheels, struts, doors and other elements that are necessary for the proper operation of the mechanism. A simple way to understand the wake and drag of a landing gear is to analyse the undercarriage as a system of cylindrical elements with different lengths and diameters that interact between them and with the doors.

2.1.1 Flow across cylinders

Circular cylinders have always been an important area of attention in aerodynamics due to its engineering significance and simplicity of the geometry. The flow structure around cylinders is dependent on Reynolds number.

The total drag is composed by the pressure drag and skin friction drag [3]. The pressure drag is the result, in the freestream direction, of the forces acting normal to the surfaces of the geometry. The normal force or pressure is the static pressure of the fluid at each position so is related to the speed of the fluid at that point. The maximum static pressure is in the stagnation point where the fluid is still. From the stagnation point the fluid begins to accelerate around the object, for a cylinder in an inviscid fluid the maximum speed is located where the maximum thickness is. The skin friction drag is the result of the forces parallel to the surface. The normal force is the consequence of the viscosity and the no-slip

condition between the body and the fluid. Due to the velocity gradient that is formed between the steady fluid attached to the body and the freestream a shear force is generated proportional to the viscosity of the fluid.

Another phenomenon that has an impact in the total drag in real flows is the boundary layer. The boundary layer is related to the viscosity of the fluid as the boundary layer is known as the region where the speed of the fluid is different from the freestream. This happens near the wall and the boundary layer grows from the stagnation point. The importance of the boundary layer is that it changes the effective shape of the object, so the pressure distribution is disturbed changing the pressure drag. Other properties of the boundary layer are also important, for example the flow will separate from the body and the separation point will be dependent on the nature of the boundary layer.

The boundary layer can be either laminar or turbulent. A laminar boundary layer has a lower velocity gradient at the wall and the path lines of the fluid elements are smooth and parallel. However, the layers for a turbulent flow are very irregular and the fluid of the higher layer mixes with the fluid near the wall energizing this region. The effects of this agitation are that the velocity gradients near the wall are higher resulting in a higher skin friction drag but the separation will occur later for the same reason (see Figure 2.1.1). Hence, for a slender body is interesting to have laminar flow as the dominant type of drag is the skin friction drag while on blunt bodies, with separation, the pressure drag is more important, so a turbulent flow is desirable.

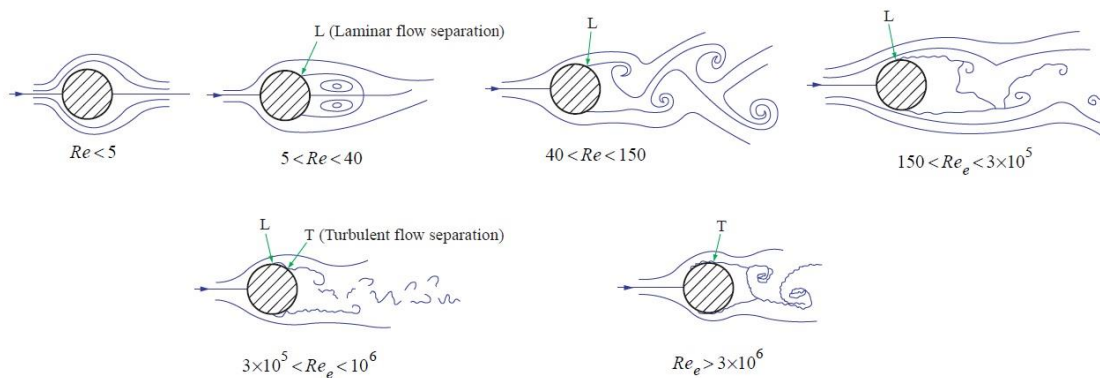


Figure 2.1.1. Flow separation mechanism on a cylinder for different Reynolds number [4]

The nature of the boundary layer is defined by its transition point, being the point where the boundary layer changes from laminar to turbulent. The distance from the leading edge, or stagnation point in the case of a cylinder, to the transition point depends on the following characteristics:

- Surface roughness: The roughness of the surface promotes the turbulent flow, thus reduces the drag of cylindrical bodies.
- Turbulence in the freestream: In a typical atmosphere the turbulence intensity reduces with the altitude, in computational fluid dynamics this value can be chosen when defining the properties of the farfield.
- Pressure gradients: Adverse pressure gradients, where pressure increases downstream, can cause flow separation but they also favour the transition.

Some similarity parameters that affect transition and are very common when it comes to boundary layers are:

- Mach number: High values of the freestream Mach number tend to encourage laminar flow, particularly at high-altitude hypersonic flights.
- Reynolds number: The most dominant factor, at low Mach number values as the cases analysed, is Reynolds number. The drag coefficient of cylinders is usually presented as a function of Reynolds number as shown in Figure 2.1.2. The critical Reynolds number is defined as the Reynolds number at the location of the transition, which experience has shown to be around 500,000 for practical applications.

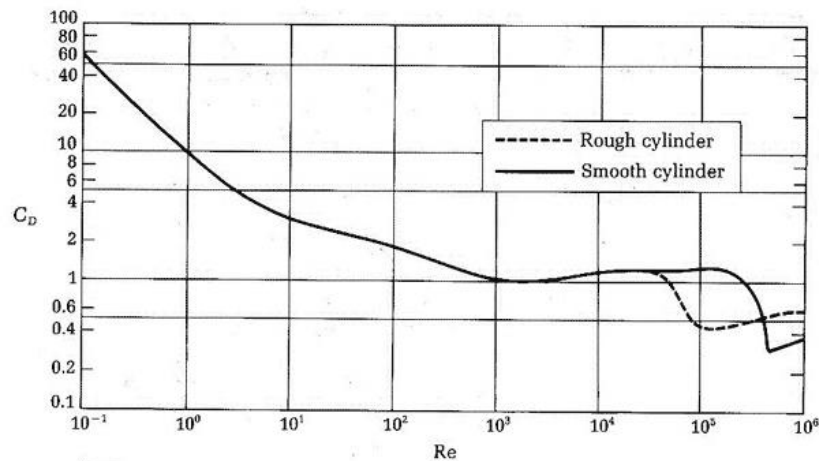


Figure 2.1.2. Drag coefficient of a cylinder as a function of Reynolds number [5]

The drag of spheres and cylinders is so well known that it is used to validate new computational codes [6] and the new lines of research are more focused on more physically accurate CFD simulations (LES or DES) [7]; [8], 3D effects [9] and different geometries as cylinder arrays or prisms.

2.1.2 Drag of flat plates

The doors of the landing gear act as flat plates parallel or perpendicular to the flow. These different arrangements of flat plates show the two extremes of the drag, pressure drag, and skin friction drag, presented in the previous section.

2.1.2.1 Flat plate parallel to the flow

Flat plates parallel to the flow are used to introduce and study the boundary layers and their development [3]. The boundary layers have already been introduced so the relation between the skin friction drag and the velocity gradient is known.

The advantage of flat plates is that it is possible to solve the boundary layer equations, which are a simplification of the Navier-Stokes equations, to get the skin friction drag using the Blasius' equation. The result shows that skin friction drag is a simple function that grows as $Re_c^{-1/2}$ (Reynolds number based on the length of the plate) for a laminar boundary layer and $Re_c^{-1/5}$ for a turbulent boundary layer (see Figure 2.1.3).

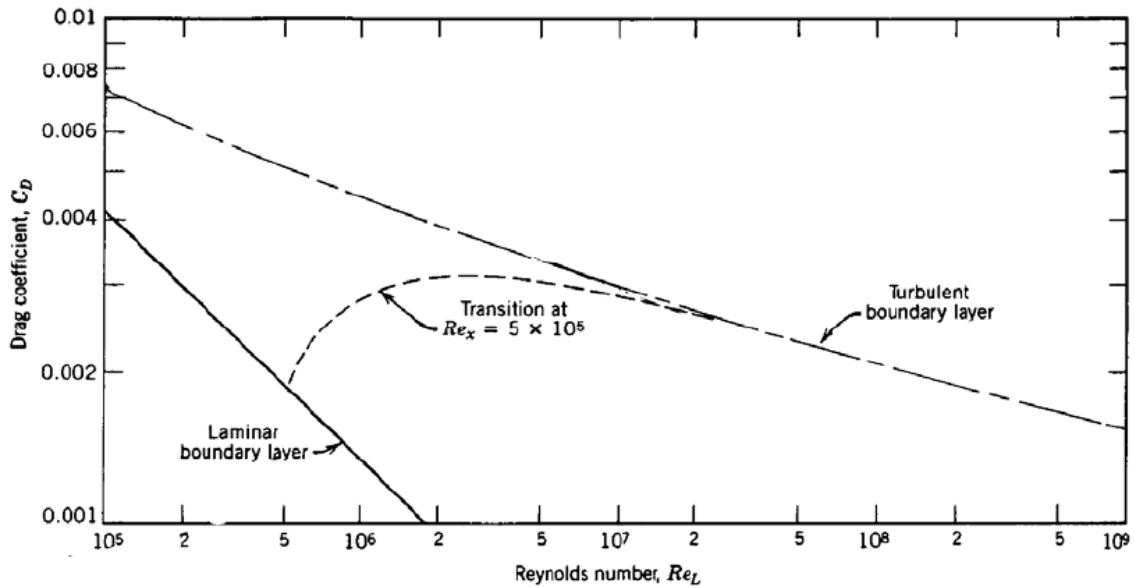


Figure 2.1.3. Drag coefficient of a flat plate [5]

2.1.2.2 Flat plate perpendicular to the flow

The rear door of the front gear is almost perpendicular to the flow, so its behaviour is comparable with a flat plate perpendicular to the flow. The drag of a flat plate is entirely due to the pressure drag as the edges perform as separation points. The fluid in the shadow of the plate is entirely detached reducing the pressure of this region and combined with the big pressures at the front of the plate results in a high pressure drag. The flow structure behind the flat plate is very complex with recirculation zones and vortices that will eventually disappear downstream.

2.1.3 Cavity flow

The last areas of interest in the landing gear system are the cavities which are classified as open, closed or transitional depending on the structure of the separation region and has been widely studied in the past decades.

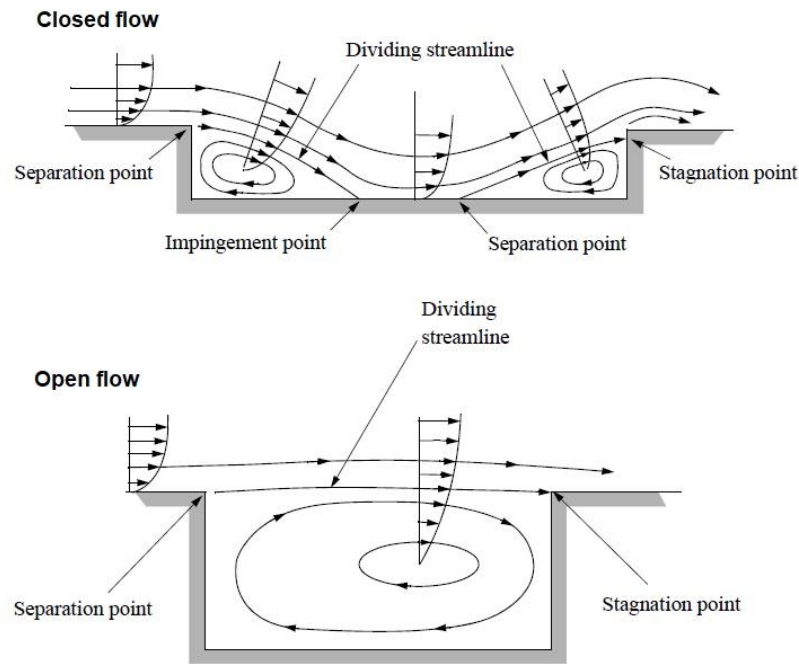


Figure 2.1.4. Closed and open cavity flows [10]

The flow will separate at the front of the cavity and the reattachment point will define the nature of the cavity as shown in Figure 2.1.4. If the flow reattaches at the floor of the cavity creating two flow separate recirculation zones, one at the front and a second at the back, the cavity is known as closed. This type of cavity is characterised by a high length to depth ratio. If the cavity is too short and the flow encounters the backward wall before the reattachment has occurred the cavity is known as an open cavity. However, the flow inside open cavities moves in a continuous circular movement.

In the recent decades the flow inside these types of cavities has been subject of many investigations specially the closed cavities. The structure of closed/shallow cavities is equal to a backward-facing step followed by a forward-facing step which are interesting because they are the simplest boundary value problems that can be formulated with the Navier-Stokes equations. Some numerical investigations of backward facing step flows [11]; [12] show the effect of different characteristics, as the height or inclination of the step, on the flow structure and pressure field. Many studies in flow control have shown that there are several techniques as plasma actuators, periodic excitation and jet and vortex generators that can be used to control the separation bubble in this type of flows [13]; [14].

Despite being less known, there are other investigations regarding 3D flows [15]; [16] that show some interesting features as pressure contours for different cavity depths and yaw angles.

2.2 Drag prediction techniques

Among all the drag prediction techniques available the following methods were used this study.

2.2.1 Empirical methods

An empirical method for undercarriage drag predictions is given in the ESDU 79015 [17], which provides a series of equations to predict the drag coefficient of each component of the landing gear for low speed flights ($M < 0.4$). This method also includes the interference between different elements of the undercarriage and other elements that are close to the gear that have and influence in the nearby flow field, such as, the wing and flaps.

2.2.2 Computational methods

Previous studies [18]; [19] analysing the Scottish Aviation Bulldog using Computational Fluid Dynamics (CFD) have concluded that the ESDU method is a good tool for the first approximation. The challenge of this project is that the landing gear of the Bulldog is fixed so the drag of the undercarriage cannot be isolated in the experimental data and a direct comparison between the experiment and ESDU is not possible. The computational methods have shown that the drag of the undercarriage is influenced by the presence of the aircraft and, although, the ESDU method applies a correction for the proximity of the wing, the entire aircraft should be considered to get better agreement with the CFD results.

2.2.3 Experimental methods

The experimental data was gathered in steady, level flights at cruise configuration (CR) and undercarriage down (UCDWN). The following procedure was followed:

- First, the aircraft was trimmed at the desired altitude and speed. This speed was the maximum speed from the desired range, for the Jetstream is around 200 and 160 knots at CR and UCDWN respectively due to the high structural forces above those speeds. The angle of attack (AoA) depends on the load factor and the speed, so for the first point the angle must be the minimum.
- Once all the data (speed, AoA, thrust and altitude) from the first point was recorded the speed was reduced to reach another stable condition at the desired speed modifying the thrust level and increasing the angle of attack. This procedure was followed until the minimum speed was reached which is around 110 knots, function of the stall speed.
- The data has continuously been generated for the last decade during more than 500 flights which allowed to estimate the lift and drag characteristics for the desired configurations. This data is going to be the reference when comparing the other two models.

2.3 Mesh generation

The mesh is necessary to define the volumetric units that the governing equations are going to be employed. The properties of each cell and their connection with adjacent cells will define the solver needed and the time to achieve a converged and physical solution. The main properties of a mesh will be introduced in the following section.

2.3.1 Mesh types

The most common type of classification is based on the mesh connectivity, how the cells are connected. This divides the possible meshes into structured, unstructured and hybrid [21].

- Structured meshes have regular connexions between cells that allows to reduce the storage space of each mesh. Another advantage of this mesh is that it has a better convergence than other types. Structured meshes are limited to simple geometries. A more flexible mesh can be obtained

dividing the domain in different blocks or mesh zones, this technique is known as multiblock.

- Unstructured meshes have irregular connexions so the storage capacity needed is larger but this types of meshes allow for any possible element available in a solver. This mesh is more flexible than the others which enables them to model any geometry.
- Hybrid meshes contain regions of structured and unstructured meshes and are more complex than unstructured meshes. In the case of fluid dynamics hybrid meshes are widely used due to the need to capture the boundary layer. The boundary layers are usually captured using a structured mesh with small cell height near the walls and an unstructured mesh around it.

2.3.2 Mesh quality

The aim of any mesh is to give precise result as quickly as possible which are opposing properties because a precise result requires many cells, and this slows down the simulation. Therefore, the quality of the mesh must be improved as this will give the optimum relation between speed and precision. Bad quality meshes can also converge but the results given might not show what is really happening around the body, one example could be where the boundary layer is not captured correctly which is the first step to measure the skin friction. Some important features to consider in order to obtain good quality meshes will be presented in this section.

One parameter that must be checked before generating the mesh is y^+ . This parameter is used to define different regions inside a boundary layer near the wall. This parameter will define the height of the first cell because if these velocity variations that occur near the wall are going to be captured the mesh size will be limited. There are some cases where the wall effects are negligible and there are some semi-empirical formulae that connect the viscous layer and the turbulent region. The value of y^+ depends on the Reynolds number so an initial guess must be made before generating the mesh and once the solution is obtained check that the value is the desired. Different turbulent models will also require different

y^+ values as they treat the turbulence in distinct ways as can be seen in the following chapter.

While y^+ is a parameter that defines the first cells of the grid there are other features that affect every cell of the mesh. Some of these parameters to measure the quality are the skewness, smoothness and aspect ratio. The skewness is the difference between the optimal cell size, a regular polygon, and the real cell size. This property applies to triangles and tetrahedral cells. The smoothness is the change in cell size between adjacent cells, a smoother mesh will have smaller changes between cells which means a better quality. The last parameter is the aspect ratio which is the ratio of the longest and shortest edges of a cell. The ideal aspect ratio is equal to one but in some cases, for example near the walls due to the maximum possible height of these cells, this is not possible.

Another technique to improve the results and assure that the solution obtained is correct is the mesh adaption and a grid independence study. The mesh adaption is a useful way to capture complex flow regions such as shock waves or separated flows. The adaption consists of refining the mesh where the desired event is likely to occur, for example behind the landing gear. The refinement of the mesh may change the results so is necessary to compare the results of different grids to find out which mesh gives good results and more refinement does not change the result. This process is known as grid independency study.

2.4 CFD of an aircraft with the undercarriage

As the mayor part of this project is to obtain results from a CFD case, in this chapter, two mayor aspects that define a model will be introduced. These are the governing equations and the turbulence model.

2.4.1 Governing equations

The first simulations, due to the lower computational power required, are going to be made using Reynolds Averaged Navier-Stokes (RANS).

Higher order methods for the drag analysis of an undercarriage as Detached Eddy Simulation (DES) and Unsteady Reynolds Averaged Navier-Stokes

(URANS) have been compared in previous studies [20] showing that both methods predict the surface pressure around the wheels accurately, while the drag differs from the experimental data. Unfortunately, DES is still computationally too expensive for such a complex model as an aircraft.

Research of unsteady separated flow [22], comparing URANS and RANS, concluded that unsteady simulation is able to capture the vortex shedding that occurs at the separated region reproducing the physics better.

2.4.2 Turbulence models

In a turbulent flow, the velocity and pressure of a fluid can be decomposed into a mean value and a varying part. The Reynolds Averaged Navier-Stokes equations are the equations that govern the mean flow, but the velocity fluctuations still appear in the nonlinear term from the convective acceleration. The nonlinear term is called the Reynolds stress.

The equations must be closed to remove the fluctuating parts so the Reynolds stress must be modelled as a function of the mean flow. The first solution was presented by Boussinesq, who introduced the concept of eddy viscosity and proposed relating the turbulence stresses to the mean flow. This hypothesis is employed in the Spalart-Allmaras, k - ϵ (k -epsilon) and k - ω (k -omega) models [23].

The Spalart-Allmaras model is a one equation model that was developed to solve aerodynamic flows and gives good results for boundary layers in adverse pressure gradients. This is a low-Reynolds number model that requires the boundary layer to be solved. The model is currently able to solve meshes independent of the near-wall y^+ because the formulation blends from a viscous sublayer formulation to a logarithmic formulation based on y^+ . However, the boundary layer should be resolved with a minimum of 10-15 cell to maintain its integrity.

The two-equation models determine the turbulence length and time scales solving two transport equations. The standard k - ϵ model is a model based on the transport equations for the turbulence kinetic energy (k) and its dissipation rate

(ϵ). This model assumes that the flow is fully turbulent, and some modifications were introduced to improve its performance, two variants being the RNG k- ϵ and the realizable k- ϵ .

The turbulence model used for the sensitivity analysis was the RNG k- ϵ , as it is more accurate and reliable for a wider class of flows. This model is like the standard k- ϵ but includes some refinements as:

- An additional term in the dissipation rate equation to improve the precision for strained flows.
- The effect of swirl on turbulence is included.
- An analytical formula for turbulent Prandtl numbers instead of constant values.
- It provides a formula for the viscosity for low-Reynolds number effects while the standard k- ϵ is a high-Reynolds number model.

Another two-equation model is the k- ω model which is based on the specific dissipation rate (ω), the ratio of ϵ to k. The formulation proposed by Wilcox considers modifications for low-Reynolds number effects, compressibility and shear flow spreading. The weak point of this model is that the solutions are sensitive to values for k and ω outside the shear layer. Some modifications were applied to improve the accuracy of the model for free shear flows.

The variant of the k- ω model studied for the undercarriage is the shear-stress transport (SST) k- ω model which includes the following refinements that make it more accurate and reliable for a wider class of flows:

- A blending function is included to activate the k- ω model near the wall and the transformed k- ϵ model away from the surface.
- Incorporates a damped cross-diffusion derivative term in the dissipation rate equation.
- Accounts for the transport of the turbulence shear stress in the turbulent viscosity.

These models will be compared with a four-equation model which is presumed to be more accurate but for a higher cost. The Transition SST model is a four-equation model based on the SST k - ω transport equations and two more, one for the intermittency and one for the transition onset.

2.5 Previous investigation with the Jetstream

The model was generated using non-contact laser scanning technology [24] and the 10th scale wind tunnel model of the Jetstream 31.

Several studies of the simplified CAD model [25]; [26], without the propellers, are available showing that the computational model gives good results at low angles of attack, as RANS is not able to predict the unsteady physics near separation as stated earlier. These studies also conclude that the computational model is closer to experimental data than the wind tunnel tests.

The latest modifications of the model are the installation of propellers [27] and the effect of different propeller models have been analysed [28]; [29]: a pair of actuator discs, a Multiple Rotating Frame Model (MRF) and a Sliding Mesh Model (SMM). Due to the complexity of the boundary conditions the MRF and SMM have not been validated, while the actuator disc shows the expected changes in the pressure distribution over the wing as seen in previous researches [30].

2.6 Other areas of interest. Aeroacoustics

Although being beyond the scope of this investigation, the literature has shown that many researches, due to the new regulations regarding airframe noise and sustainability, are investigating the noise sources and ways to reduce the intensity of it in the noisiest regions of the aircraft, one of those being the undercarriage [31]; [32]; [33]; [34]. This area of aerodynamics could be an interesting research line for future investigation.

3 METHODOLOGY

In this section it is going to be explained how the objectives were achieved, going through all the process and steps required to obtain the desired results.

3.1 Computer-aided design (CAD)

The starting point of the project was the CAD model generated by Robert Parker [24] using a scanning process explained in the literature review and saved as a project in CATIA.

The model of the aircraft at cruise configuration had to be modified as the objective of this work is to study the drag of the undercarriage. The modifications of the geometry were made using CATIA as described in the following paragraphs.

The first step, before running CATIA, was to measure the dimensions of the landing gear and decide which parts were going to be modelled, for being the most significant parts, and which parts were going to be discarded from the model because their introduction would require a very detailed mesh increasing the number of cells of the mesh and consequently the time of the simulations. The measurements of the parts were taken from the aircraft parked in the hangar. The location of the landing gear relative to the fuselage is available in the specifications of the aircraft.

The landing gear was modelled using the analytical method published by ESDU as reference, so each mechanism consists of a system of struts, doors, wheels and a cavity. This will allow to make a direct comparison between the results of the CFD and ESDU and validate both with experimental data.

The retractable landing gear consists of a front gear and the main gear, which is formed by two symmetrical mechanisms located under each wing, forming a tricycle arrangement.

The front gear (see Figure 3.1.1) is located under the cockpit and the mechanism is formed by a pair of wheels parallel to each other and connected by a shaft. The

shaft is connected to the strut which goes vertically into the cavity of the fuselage. When the gear is retracted the wheels must go inside the cavity and then the cavity is closed by a system of three doors, two lateral doors and a back door.

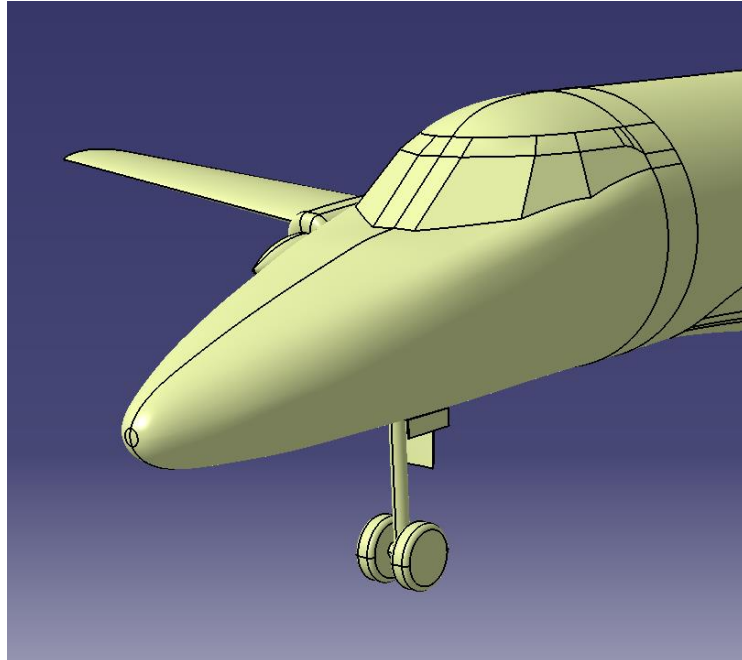


Figure 3.1.1. Front gear CAD model

Each mechanism of the main gear (see Figure 3.1.2) is located under the engines, behind the propellers, and the wheel is stowed in the root of the wing when the gear is retracted. Each system has a wheel connected to a strut that goes vertically into the cavity when it is deployed. A secondary strut is needed to pull the mechanism to the retracted position, it is barely visible from the front so that the drag of this component is minimalised. The outer element is the door that will cover the cavity partially when the landing gear is retracted, reducing the drag in cruise configuration, but the wheels will remain visible from below. The door and the strut are connected by a smaller strut, this way the door and the gear will move together using a single actuator.

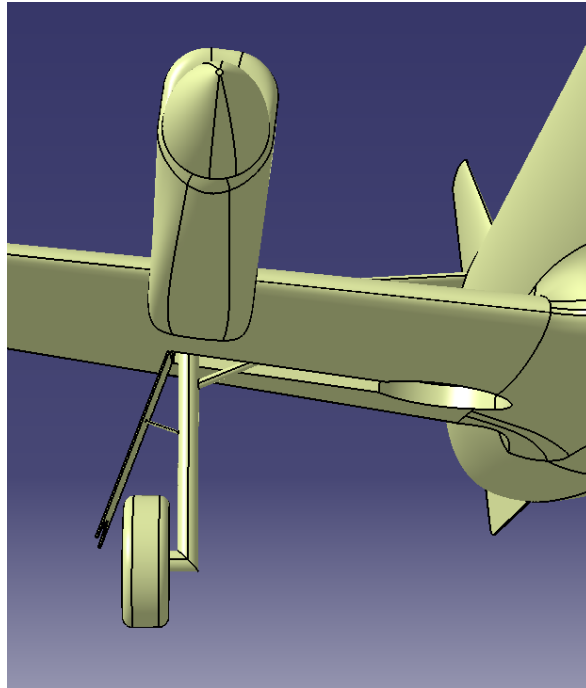


Figure 3.1.2. Main gear CAD model

The detailed dimensions of the undercarriage of the model can be seen (Part 6.2).

3.2 Mesh generation

The next phase of the project is to generate a mesh, essential to run any computational solver. The mesh generation tool used for this project was ICEM CFD, so the geometry created in CATIA was converted into an IGES file and then imported to ICEM CFD.

The first step before defining the characteristics of the mesh is to check the holes and unconnected vertices as during the process of moving the geometry from one software to another some gaps might appear. These errors can be repaired using the geometry editing tools provided by the software.

Once the geometry is repaired the parts of the aircraft were defined to allow to control the size of the mesh elements of each part. The aim is to have smaller elements where the flow is likely to be complex for example around the landing gear. Other important regions, where the mesh will be finer, are the leading and trailing edges of the wings and stabilizers.

Another important region of a mesh is the prism layer that will grow from the surface and will be responsible for capturing the boundary layer. The height of the first cell will define the quality this area which must be estimated from the desired y^+ value. Previous studies with the same aircraft [30] have shown that $y^+ = 50$ is enough to obtain similar results as those with lower values of y^+ . Applying the formula that relates this parameter with the first cell height, a height of 0.25 mm was chosen for the first cell. In order to solve the entire boundary layer, an exponential law was applied to the height of the next ten layers with a height ratio of 1.2.

Prior to importing the mesh into Fluent its quality must be checked targeting a minimum quality of 0.3. Every mesh used in the following analysis has been smoothen with the tools provided in ICEM CFD, obtaining meshes with less than 1% of their cells below the threshold value.

Finally, the mesh was refined in several stages using smaller surface cells in the undercarriage and nearby regions from 9 million cells to 14 million. These meshes will be analysed in the mesh dependency study to decide which mesh gives good enough results for the minimum number of cells.

3.3 Computational fluid dynamics (CFD)

The models had to simulated using a CFD solver and the results obtained are were analysed using a post-processor. The solver used was Fluent and the post-processor CFD-Post.

3.3.1 Solver

The simulations were run in Fluent 19.1 and aided by the High-Performance Computer (HPC) of Cranfield to reduce the time of each simulations. The farfield was defined to match the conditions (pressure and temperature) of the flight tests, changing the Mach number and angle of the incoming flow to cover a wide variety of conditions to validate the model.

The total lift and drag were monitored as well as the drag of the landing gear to check the convergence of the model. The convergence criteria were reached

when the values monitored reached a stable value. The oscillations of these values for the cases with the undercarriage were bigger giving a higher uncertainty of the solution. These variations were around 1% for the drag and convergence was reached after 3,000 iterations for most of the angles of attacks calculated.

3.3.2 Post processor

The solutions were processed using CFD-Post because it is a more efficient tool than the post processor of Fluent. It is possible to obtain forces, contours and flow visualisation from the data calculated with Fluent.

3.3.3 Mesh dependency study

A CFD model requires an analysis to ensure that the results obtained are not dependent on the mesh or turbulence model chosen. In this chapter, the steps followed until the results were obtained will be presented and the election of the mesh and turbulence model will be based on the compromise between the accuracy and computational cost.

The mesh dependency study was made for different mesh densities that are characterised by the number of cells as the control volume is the same for any mesh. A medium density mesh with 10 million cells was used as a first approach and this was modified to obtain coarser and finer meshes until a convergence between consecutive meshes was reached. The refinement was done reducing the surface mesh size around the landing gear as this is the most interesting region for this project and the mesh size of previous studies was used for the rest of the plane. The convergence was checked comparing the lift and drag of the whole model and the drag of each new system added to the previous model which are the front gear and the main gear. Once the difference between two consecutive results is in the order magnitude of the accuracy of the results the analysis had converged, and no more refinement is needed.

The same case was simulated for every mesh which corresponds to an intermediate case from the range of angle and speeds programmed. The simulations were made for a Mach number of 0.25 and AoA of 5°.

	Nº of cells (millions)	Cl		Cd	
		value	difference with Extra Fine	value	difference with Extra Fine
Very Coarse	8.8	0.874	2.8%	0.0862	6.4%
Coarse	9.7	0.862	1.4%	0.0832	2.7%
Medium	10.9	0.861	1.3%	0.084	3.7%
Fine	11.8	0.855	0.6%	0.081	0.0%
Very Fine	13.1	0.85	0.0%	0.081	0.0%
Extra Fine	13.9	0.85	0.0%	0.081	0.0%

	Nº of cells (millions)	Front gear drag		Main gear drag	
		value	difference with Extra Fine	value	difference with Extra Fine
Very Coarse	8.8	0.0100	0.2%	0.0105	26.0%
Coarse	9.7	0.0096	-4.5%	0.0095	14.5%
Medium	10.9	0.0102	2.0%	0.0100	19.9%
Fine	11.8	0.0097	-3.0%	0.0085	2.4%
Very Fine	13.1	0.0095	-5.0%	0.0090	8.4%
Extra Fine	13.9	0.01	0.0%	0.0083	0.0%

Table 3.3.1. Lift and drag variations with different mesh densities

The fine mesh is the one that satisfies the condition of a good accuracy for the minimum cost (see Table 3.3.1) as the error in the global lift and drag is below 1% and the drag of the components is the closest to the finest mesh. All the details of the mesh are shown in Appendix A.

3.3.4 Turbulence model study

A similar study was made for different turbulence models, using first and second order methods in case there were differences. The one and two equation models were compared with the 4-equation model Transition SST, introduced in the literature review, which should be the most accurate but also computationally expensive.

		Cl		Cd	
		value	difference with Transition SST	value	difference with Transition SST
Espalart-Almaras (1 eq)	2nd order	0.855	1.8%	0.081	3.8%
k-e RNG (2 eq)	1st order	0.78	-7.1%	0.074	-5.1%
	2nd order	0.79	-6.0%	0.074	-5.1%
k-w SST (2 eq)	2nd order	0.84	0.0%	0.078	0.0%
Transition SST (4eq)	1st order	0.82	-2.4%	0.078	0.0%
	2nd order	0.84	0	0.078	0

		Front gear drag		Main gear drag	
		value	difference with Transition SST	value	difference with Transition SST
Espalart-Almaras (1 eq)	2nd order	0.0097	5.4%	0.0085	-1.2%
k-e RNG (2 eq)	1st order	0.0085	-7.6%	0.0085	-1.2%
	2nd order	0.0088	-4.3%	0.0081	-5.8%
k-w SST (2 eq)	2nd order	0.0096	4.3%	0.0086	0.0%
Transition SST (4eq)	1st order	0.0095	3.3%	0.0086	0.0%
	2nd order	0.0092	0	0.0086	0

Table 3.3.2. Lift and drag variations with different turbulence models

The analysis of the turbulence models showed that the results obtained with the turbulence model $k-\omega$ SST are almost the same as the 4-equation model as can be seen in Table 3.3.2 but for a lower computational cost. The final setup of Fluent can be seen in the Appendix B.

3.4 Validation of results

To validate the model, the results obtained from the CFD will be compared with other methods of drag estimation and flight test data. These comparisons will be presented in the next section.

4 UNDECARRIAGE DRAG ANALYSIS

In this section the results obtained with the different methods will be presented.

4.1 CFD model

In the following section the flight test data is compared to the different drag prediction methods used, the CFD model and empirical models. The discrepancies between the models will be presented, along with the results.

4.1.1 Cruise configuration

The results presented in this were obtained using the same set up that has previously been studied [26]. The new results obtained show the same result that support the conclusions reached in the previous studies. The following charts show the comparison between the lift and drag characteristics at cruise configuration obtained from the flight tests and the CFD model.

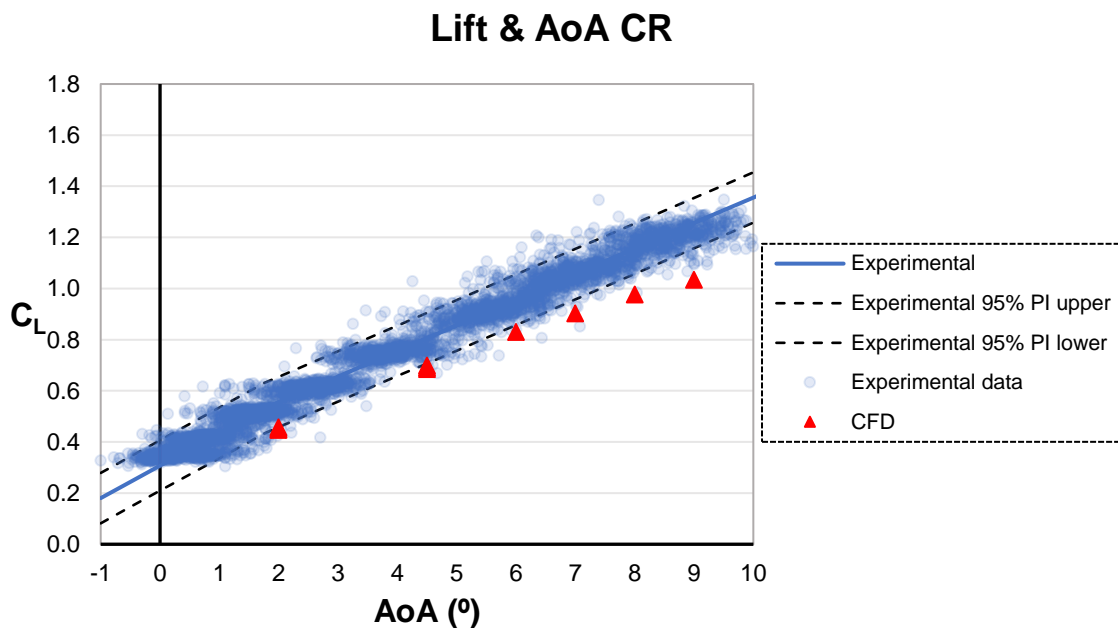


Figure 4.1.1. Lift characteristics at CR configuration

Figure 4.1.1 shows the variation of the lift coefficient with the angle of attack based on the body reference line. The lack-of fit test has shown that the approximation of the data with a singular line does not predict correctly the data for low angles of attack. Therefore, the flight test data was approximated by two

linear fits, the transition happens around 1.75° . The first curve follows the equation $C_L = 0.3079 + 0.1276\alpha$ while the second has a more moderate slope, $C_L = 0.3561 + 0.1\alpha$. The result obtained from CFD fall just below the prediction intervals, estimating less lift than the measured on the aircraft. Another difference can be seen at high angles of attack as the model predicts the onset of separation earlier than the flight tests.

These discrepancies are likely to be caused by the absence of propellers on the CFD model. Some previous studies have shown that the predictions improve when the propellers are included [27]; [28]; [29]. The effect of the propellers is that the flow across them is accelerated increasing the local dynamic pressure, thus, the lift is incremented locally in the slipstream of the propellers [26].

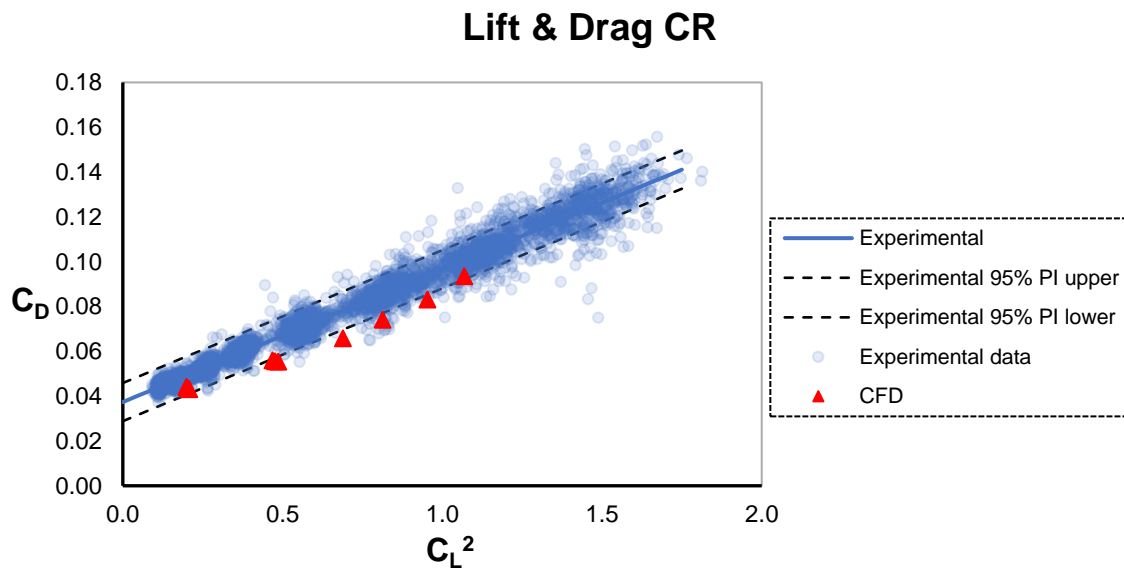


Figure 4.1.2. Drag polar at CR configuration

Figure 4.1.2 shows the linear section of the drag polar. The drag in this region is governed by the drag polar equation:

$$C_D = C_{D0} + \frac{C_L^2}{\pi A R e} = C_{D0} + k C_L^2$$

where, C_{D0} is the drag coefficient at zero lift and $k C_L^2$ is the drag due to lift, which depends on the aspect ratio (AR) and the efficiency factor (e).

The best fit line for the experimental data is $C_D = 0.0374 + 0.0593C_L^2$ which is again above the CFD model.

The difference in drag may arise from the same origin as the differences in lift which are the propellers. As stated, the propellers increase the lift, so the drag due to lift should also increase locally if the propellers were included. Another effect of the acceleration of the flow is that the skin friction coefficient will increase leading to an increase in the zero lift drag coefficient. Therefore, the incorporation of the propellers should improve the drag estimates.

4.1.2 UCDWN configuration

The results presented in this chapter were obtained with the mesh analysed previously that contains the landing gear. These results obtained from the simulations are presented with the experimental data gathered from level accelerations.

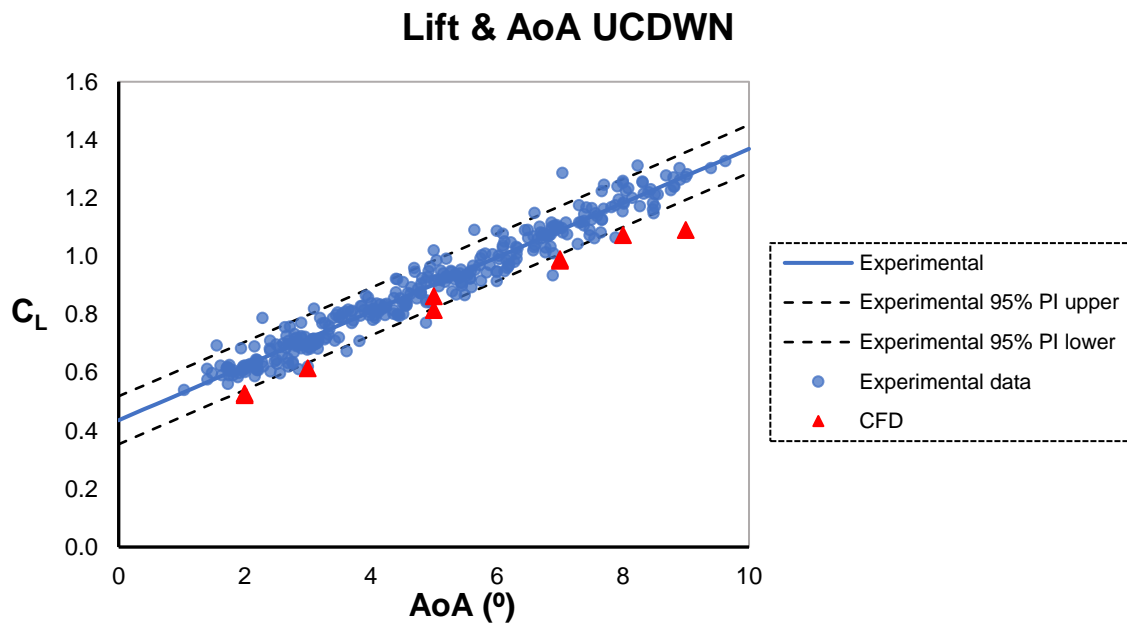


Figure 4.1.3 shows the lift coefficient variation with the angle of attack with the landing gear down. The linear fit follows the equation $C_L = 0.436 + 0.093\alpha$. The lift coefficient of the CFD model is slightly lower than the experimental data, but the results are within the prediction intervals. As the previous case, the onset of

separation, which begins to occur at angles of attacks higher than 6° around the root of the wing as can be seen in the figures of Appendix D, is predicted earlier in the computational model and the same explanation as for CR configuration can be given for the difference. The addition of the propellers should increase the lift and improve the CFD estimates, particularly at high angles of attack.

If the lift equation of UCDWN configuration and CR configuration are compared, the lift generated with the undercarriage down is higher. For an angle of attack of 2° , the lift increment from the experimental data is around 10% while CFD gives an increment of 15%. Analysing the data obtained from the simulations, was seen that the difference comes from the lift generated by the wing as the new components of the model do not generate lift. In order to identify the source of the difference the spanwise vertical force has been plotted, which is equivalent to the lift coefficient for $\alpha=2^\circ$ (see Figure 4.1.4) The results show that the coefficient is higher in the proximity of the main gear, so the presence of the landing gear affects the pressure field under the wing.

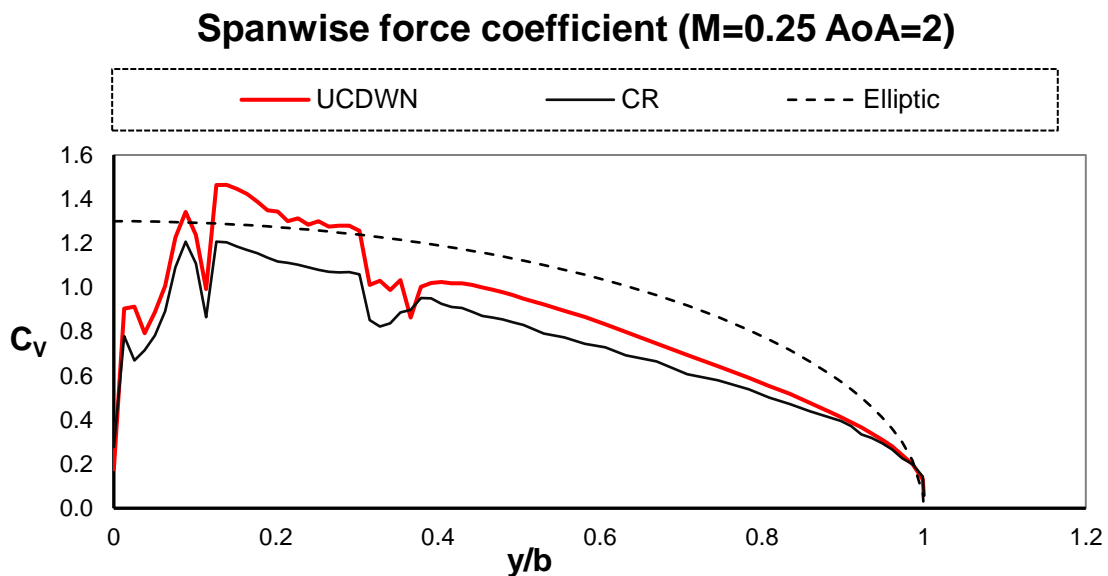


Figure 4.1.4. Spanwise vertical force coefficient comparison

The pressure contours from Figure 4.1.5 show nearly any variations in the upper surface, while the pressure below the wing is modified, mostly due to the wake of the strut and a higher pressure inside the cavity. What is more, the flow visualisation below the wing (see Figure 4.1.6) shows that the streamlines behind

the nacelle are displaced towards the tip due to the presence of the door and the flow is detached inside the cavity as the streamlines do not follow a regular path and the shear stress is almost null. These phenomena increase the lift generated between the fuselage and the nacelle, however, the addition of propellers is likely to reduce this effect as they also influence the total lift as discussed earlier.

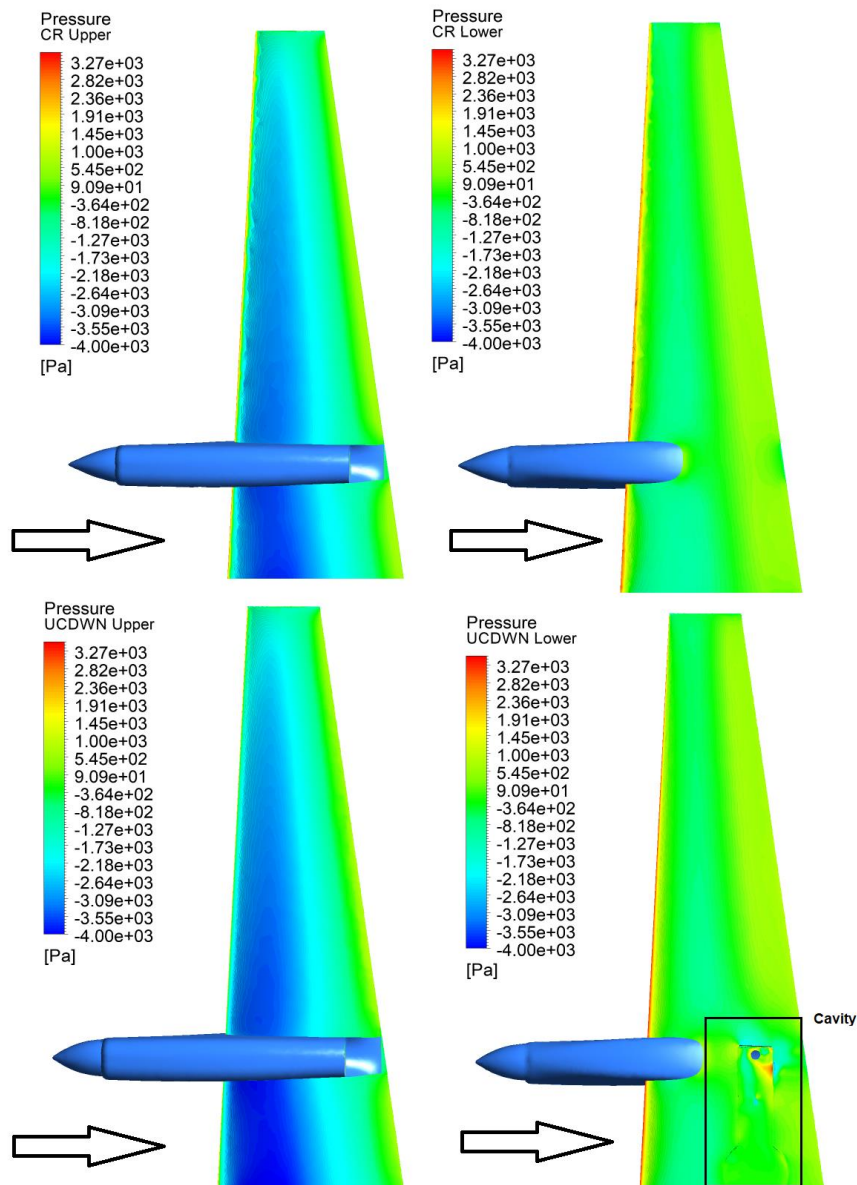


Figure 4.1.5. Pressure contours of the wing at CR and UCDWN configurations, where the arrow shows the freestream flow direction. ($M=0.25$, $\alpha=2^\circ$)

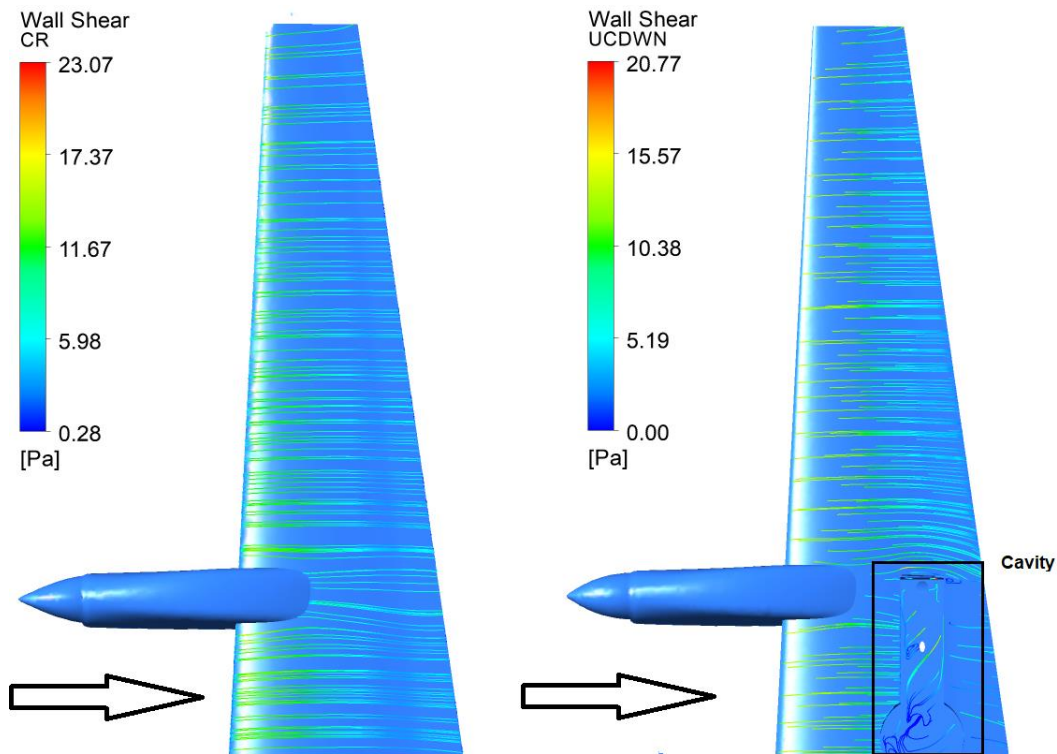


Figure 4.1.6. Flow visualisation of the lower surface of the wing, where the arrow indicates the direction of the freestream flow. ($M=0.25$, $\alpha=2^\circ$)

Lift & Drag UCDWN

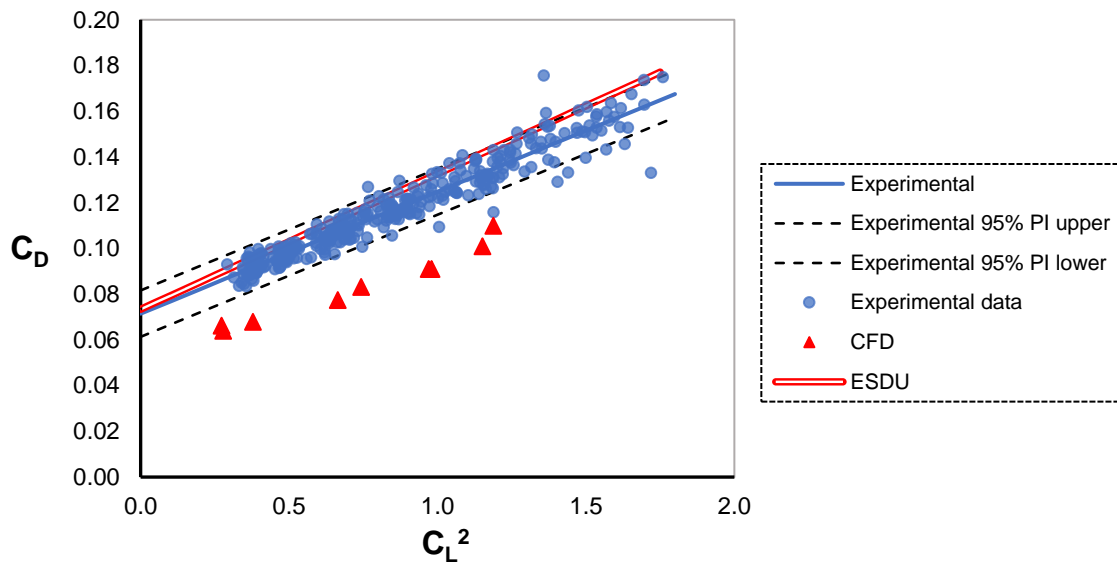


Figure 4.1.7. Drag polar at UCDWN configuration

Figure 4.1.7 shows the drag polar with the landing gear down. In the figure, the results of the three methods used are presented: experimental data from level-flight accelerations, the results of CFD and the drag predicted with the ESDU method.

The experimental data is approximated with a linear fit, as the drag is assumed to increase according to the empirical equation $C_D = C_{D0} + KC_L^2$. For the case studied the equation obtained is: $C_D = 0.0715 + 0.0533C_L^2$. Comparing this equation with the drag at cruise, the increment in the zero-lift drag is $\Delta C_{D0} = 0.0341$, whose source is the undercarriage. The slope of the linear fit, which is inversely proportional to the aspect ratio of the wing and the efficiency factor of the lift distribution, is lower than the slope at CR. Considering that the aspect ratio is constant, as the wing has the same dimensions, the only variable that can be changed is the efficiency factor. This factor increases while the lift distribution gets closer to an elliptic distribution. Analysing the Figure 4.1.4, the results show that the lift distribution is closer to the elliptic distribution when the undercarriage is down and the drag polar obtained from CFD supports this conclusion.

The drag polar obtained from CFD has a lower slope until the separation begins to occur. Following the same line of thinking, these different is possibly because the propellers modify the spanwise lift distribution reducing the efficiency factor. However, the biggest discrepancy between CFD and experimental data is that the drag is underpredicted. A closer analysis of the drag has shown that the drag predictions of the first model (CR) and the second (UCDWN) without adding the drag of the landing gear follow the same trend, meaning that the drag of the whole aircraft is underpredicted. Knowing that the drag of the aircraft and the undercarriage are added, and both estimates are underpredicted, the error of the total drag will be the sum of the error of each element leading to the difference shown in Figure 4.1.7. The drag coefficients of each element can be seen in the tables of Appendix C.

The drag may also be underpredicted due to the simplified nature of the computational model. There are many elements in the landing gear that were not modelled due to the complexity of the model in that case.

The red line, called ESDU, was generated adding the drag calculated with empirical methods and the drag equation of the cruise configuration. The prediction is inside the prediction interval, but in this case overpredicts the drag and it is not possible to predict the change in the slope of the drag curve. Another

issue with this method is that it does not predict the increase in lift that was analysed for the other cases.

4.2 ESDU method

In the previous section was introduced that the total drag is underpredicted because the drag of the aircraft and the undercarriage are underpredicted. In this chapter the drag of each element of the landing gear is going to be estimated using the method proposed by the ESDU [4] and the drag of each mechanism is going to be compared with the CFD model.

There is a system of simple equations given by ESDU to predict the drag when the dimensions of the undercarriage are known. These equations allow the estimation the drag of each component independently considering the interaction with other elements. The equations have been validated with wind tunnel data.

For the basic calculations, the gear is positioned normal to the flow. Then, the correction factors for the angle of attack are applied for the struts and doors, and the correction factors due to the presence of the undercarriage and proximity of the wing, as the main gear is located bellow the wing.

The dimensions of the gear were taken manually from the plane parked in the hangar. The same dimensions were used to build the CFD model so that both could be compared.

The drag coefficient of each undercarriage unit is calculated as described in the following equation and then they are summed to give the total undercarriage drag:

$$\frac{D_u}{qS} = \sum \frac{D_{uu}}{qS}$$

in which,

$$\frac{D_u}{qS} = \left[\frac{D_w}{qS} + \frac{D_s}{qS} + \frac{D_d}{qS} + \frac{D_c}{qS} + \frac{D_{ex}}{qS} \right] F_1 F_2$$

where D_w/qS is the drag coefficient of the wheels,

D_s/qS is the drag coefficient of the struts,

D_d/qS is the drag coefficient of the undercarriage doors,

D_c/qS is the undercarriage bay cavity drag coefficient,

D_{ex}/qS is the drag coefficient of the additional components,

F_1 is a factor for the influence of wing thickness on undercarriage drag,

and F_2 is a factor for the influence of flap deflection on undercarriage drag.

4.2.1 Front gear drag

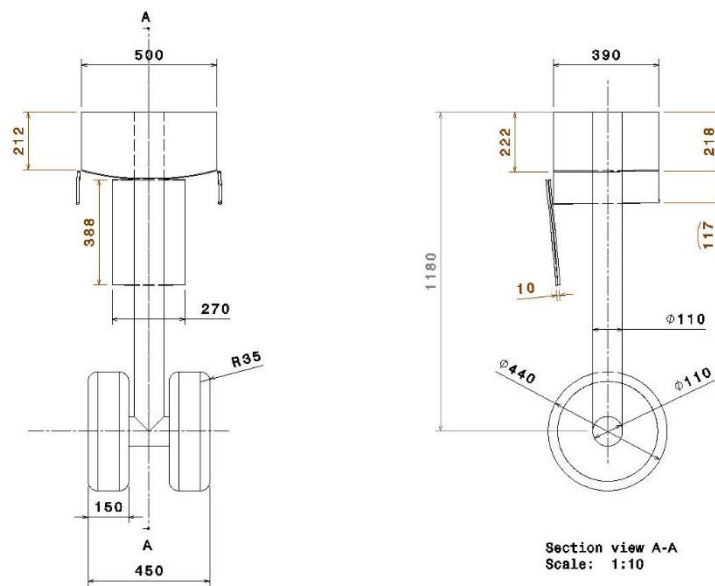


Figure 4.2.1. Dimensions of the front gear (in mm)

The front gear consists of a pair of wheels, a strut, three doors and a cavity (the dimensions of the front gear are shown in the Figure 4.2.1). It is mounted below the nose of the aircraft so there is no interaction between these components and the wing or flaps, so the general equation is reduced to the following expression:

$$\frac{D_{Front}}{qS} = \frac{D_w}{qS} + \frac{D_s}{qS} + \frac{D_d}{qS} + \frac{D_c}{qS}$$

It is worth mentioning that the drag of the additional components is not considered because the CFD model does not contain those components to simplify the mesh and reduce the time of the simulations. This will lead to an error when comparing

these results with the experimental data, the ESDU giving lower values of the drag. For the additional components, such as landing lamps, brackets and tail skids, ESDU proposes a drag coefficient of 2.0 based on the area of these elements.

4.2.1.1 Pair of wheels

The front gear has a pair of wheels parallel to each other and connected to the strut by the shaft. This arrangement is known as multi-wheel combination and the drag coefficient is estimated using the following expression:

$$\frac{D_w}{qS} = \frac{C_D}{C_{D0}} C_{D0} \frac{(bd_t - mn)}{S}$$

in which C_D/C_{D0} is obtained from the Figure 1 of (ESDU reference), function of the Reynolds number and d_w/b ,

and $C_{D0} = 1.2$ for subcritical Reynolds numbers

or $C_{D0} = 0.65$ for supercritical Reynolds numbers

The Reynolds numbers of all the simulations are above 5×10^5 so the value of the C_{D0} must be 0.65. As all the values are known the resultant drag of the pair of wheels is:

$$\frac{D_w}{qS} = 0.55 \times 0.65 \times \frac{(0.45 \times 0.44 - 0.15 \times 0.165)}{25.08} = 2.47 \times 10^{-3}$$

4.2.1.2 Strut normal to the flow

The drag of circular section struts is closely represented by a long circular cylinder, so the drag coefficient is dependent on Reynolds number and roughness of the surface. However, for very rough cylinders the drag coefficient becomes almost independent of Reynolds number and because the strut has many other elements attached to it, in practice, a drag coefficient of 1.2 is used. Thus,

$$\frac{D_{si}}{qS} = C_{Ds} \frac{l_s d_s}{S}$$

where, $C_{Ds} = 1.2$ and l_s and d_s are the length and diameter of the strut.

Substituting the values:

$$\frac{D_{si}}{qS} = 1.2 \times \frac{0.74 \times 0.11}{25.08} = 3.89 \times 10^{-3}$$

The drag of the isolated strut must be correct due to the inclination to the flow direction, R_1 , the presence of other struts, R_2 , and due to the presence of plane surfaces, R_3 . This means that the final drag is:

$$\frac{D_s}{qS} = \frac{D_{si}}{qS} R_1 R_2 R_3$$

The front gear has a single strut so, $R_2 = 1$ and the distance between the doors and the strut is large enough to ignore the interference between these elements, $R_3 = 1$. The inclination factor can be useful to modify the drag coefficient of the strut with the angle of attack and is given by $R_3 = \cos^3|\alpha|$, so for the angles of attack studied in this report it changes from 1 at 0° to 0.955 at 10° . Therefore, the values obtained in this chapter will correspond to the 0° case, without any correction factor applied, but the drag of the struts was reduced with the corresponding correction factor for the other cases.

4.2.1.3 Doors

The doors of the front gear can be classified in two types: parallel to the freestream, called lateral doors, and normal to the freestream, called back door.

The drag of the doors that are parallel to the flow consists of two components: pressure drag due to the thickness and the skin friction drag. The drag is therefore obtained from:

$$\frac{D_d}{qS} = C_{Dd} \sum \frac{t_d w_d}{S} + C_{Fd} \frac{S_{wet}}{S}$$

where $C_{Dd} = 1.0$ for a blunt leading-edge

and t_d and w_d are the thickness and the width of each door

C_{Fd} is the mean skin friction coefficient for the doors from ESDU 68020

and S_{wet} is the total door wetted area

The drag of each lateral door is therefore:

$$\frac{D_{ld}}{qS} = 1 \times \frac{0.01 \times 0.117}{25.08} + 0.0035 \times \frac{2 \times 0.117 \times 0.39}{25.08} = 0.06 \times 10^{-3}$$

The drag of the back door can be calculated using the theory of flat plates normal to the flow, explained in (reference ESDU 70015). In this case, the door is installed near the surface of the fuselage, so the drag coefficient can be estimated using the expression of the normal force coefficient:

$$\frac{D_{bd}}{qS} = C_N \frac{bc}{S}$$

where C_N is the normal force coefficient, from the figure 7 (ESDU 70015)

and b and c are the width and the height of the door

$$\frac{D_{bd}}{qS} = 1.16 \times \frac{0.27 \times 0.388}{25.08} = 4.84 \times 10^{-3}$$

So, the total drag of the doors is:

$$\frac{D_d}{qS} = 2 \times \frac{D_{ld}}{qS} + \frac{D_{bd}}{qS} = (2 \times 0.06 + 4.84) \times 10^{-3} = 4.96 \times 10^{-3}$$

4.2.1.4 Cavity

The drag coefficient of the cavity is based on the exposed area, so it must be modified for the reference area of the aircraft. The drag coefficient is therefore,

$$\frac{D_c}{qS} = C_{Dc} \frac{l_c w_c}{S}$$

in which l_c and w_c are the length and width of the cavity, and the C_{Dc} is function, also, of the depth (Figure 7 ESDU).

$$\frac{D_c}{qS} = 0.0225 \times \frac{0.39 \times 0.5}{25.08} = 0.17 \times 10^{-3}$$

Having calculated the drag coefficients of each component of the front gear the total drag coefficient can be obtained:

$$\frac{D_{front}}{qS} = \frac{D_w}{qS} + \frac{D_s}{qS} + \frac{D_d}{qS} + \frac{D_c}{qS} = (2.47 + 3.89 + 4.96 + 0.17) \times 10^{-3} = 0.0115$$

FRONT GEAR

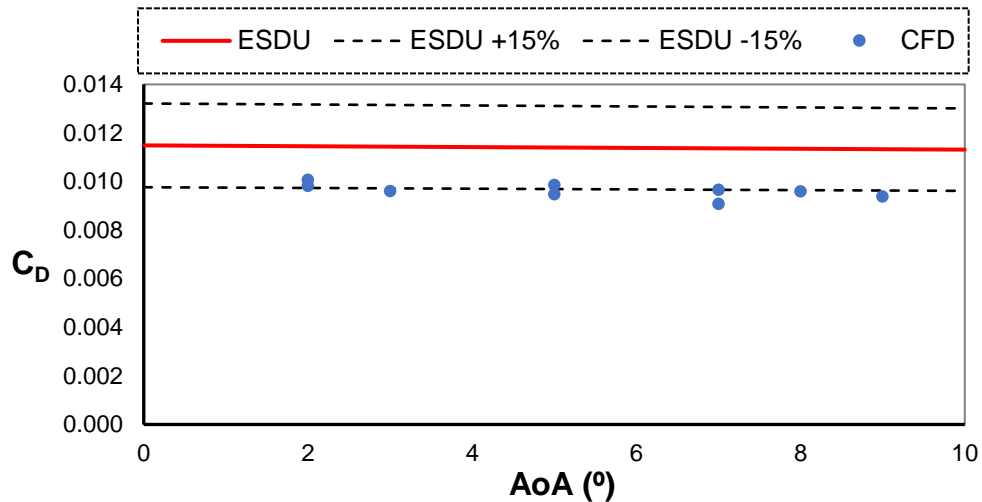


Figure 4.2.2. Front gear drag estimates, ESDU and CFD.

Figure 4.2.2 shows the drag coefficient estimates using the empirical equations, the red line, and the results from CFD. The figure shows that the total drag reduces with the angle of attack due to the reduction in the drag of the struts. However, the contribution of the struts to the total drag is so small, that the reduction of their drag of almost 5% translates into a reduction of less than 2% of the total drag.

Comparing the ESDU estimates and the CFD, the computational model underestimates the drag, but the points are still in the confidence intervals of $\pm 15\%$ proposed by ESDU. Another conclusion could be that the drag is constant for the range of angles analysed. The main reason for this is the presence of the aircraft. If the landing gear was isolated, the incoming flow would have the angle of attack defined in the farfield [19] so the drag of the strut should reduce as the frontal area is smaller. The opposite effect should occur in the cavity as the frontal area increases with the angle of attack. However, when the whole aircraft is introduced, the angle of the flow that the components of the undercarriage are facing is smaller than the angle of attack. The front gear is influenced by the deflection of the flow at the nose (see Figure 4.1.1) so the effective angle is nearly

0° for the front gear. A deeper analysis of the forces of each component support this hypothesis because the drag coefficient of each component is constant in the range of angles studied.

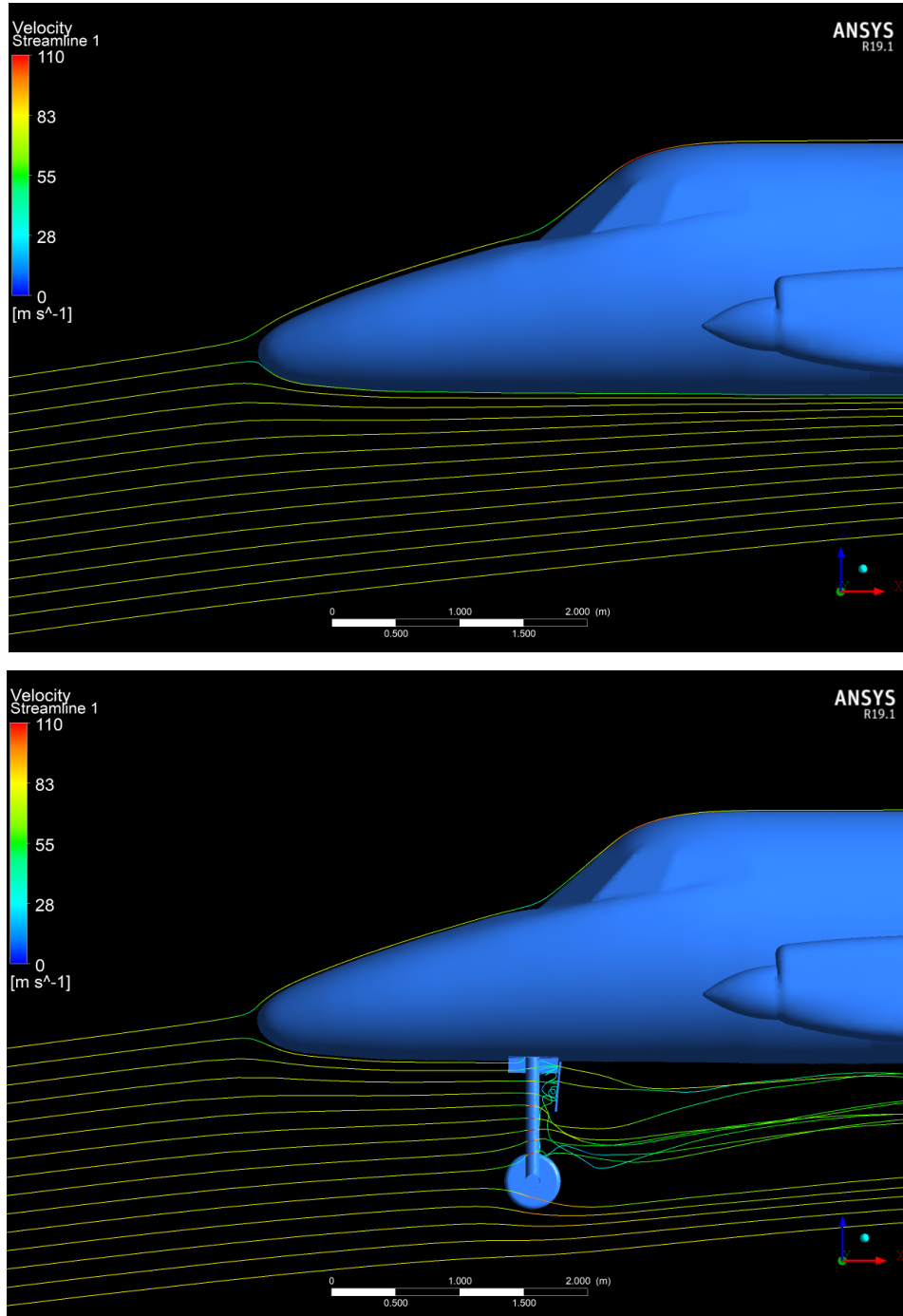


Figure 4.2.3. Flow past the nose of the aircraft at CR and UCDWN respectively, $M=0.25$ $\alpha=7^\circ$

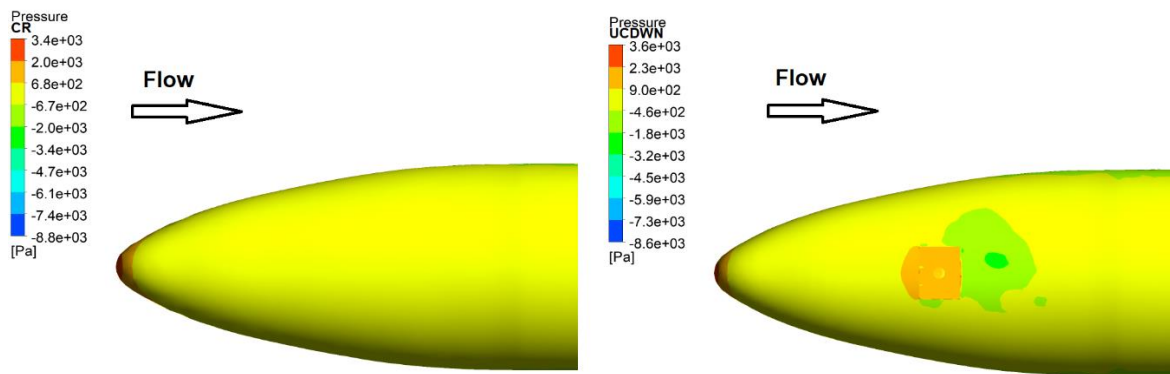


Figure 4.2.4. Pressure contours for CR and UCDWN configurations, $M=0.25$ $\alpha=7^\circ$

The pressure contours of the Figure 4.2.4 show the influence of the landing gear bellow the fuselage. The area affected can also be seen in the surface flow visualization of the Appendix D, where the streamlines are shifted to the side of the fuselage mostly due to the presence of the back door. What is more, the effect of the landing gear is visible inside the cavity, where the pressure is higher, and right behind it because the flow accelerates passing through the gap between the fuselage and the door.

4.2.2 Main gear drag

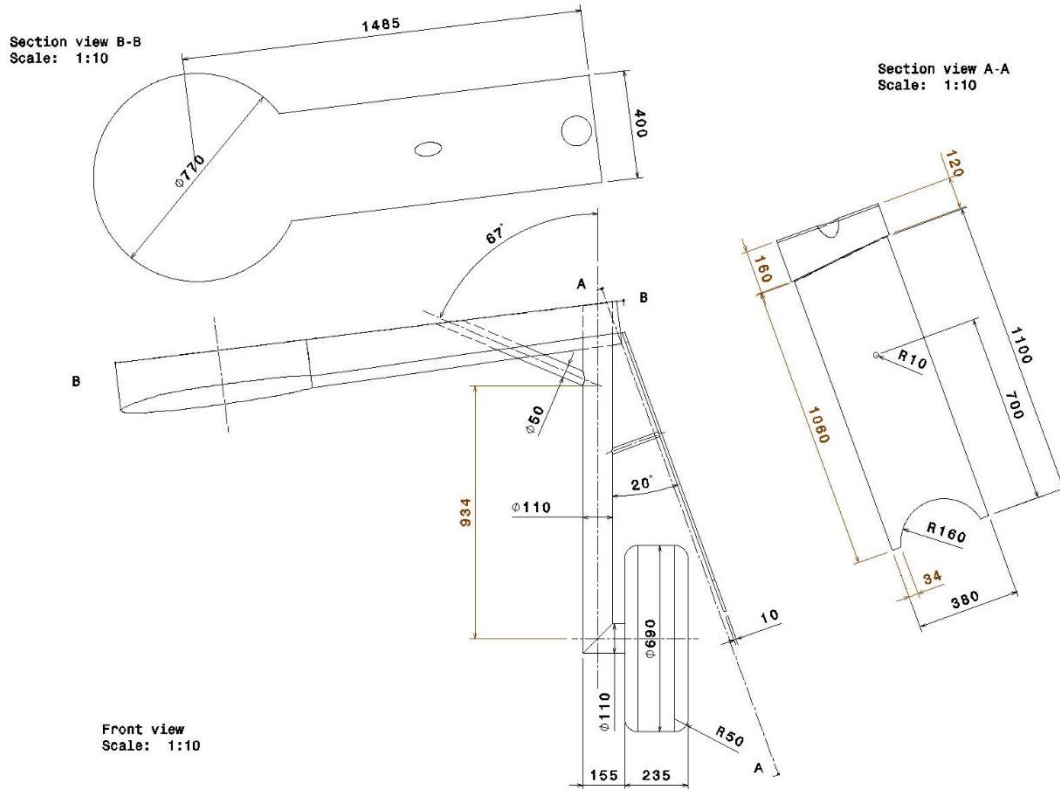


Figure 4.2.5. Dimensions of the main gear (in mm)

The main gear consists of two mechanisms, one on each wing mounted below the engines (the dimensions of the main gear are shown in Figure 4.2.5). These mechanisms are formed by single wheels and a system of struts with a door parallel to the flow as can be seen in Figure 4.2.5.

Following the same procedure as in the previous section the drag of the main gear can be estimated with the following equation:

$$\frac{D_{main}}{qS} = 2 \left[\frac{D_w}{qS} + \frac{D_s}{qS} + \frac{D_d}{qS} + \frac{D_c}{qS} \right] F_1$$

4.2.2.1 Wheel

The wheel of the main gear is in the presence of a strut and a supercritical Reynolds number. The equation of the drag coefficient for this case is:

$$\frac{D_w}{qS} = \frac{C_D}{C_{D0}} C_{D0} \frac{bd_w}{S} = 0.4 \times 0.65 \times \frac{0.235 \times 0.69}{25.08} = 1.68 \times 10^{-3}$$

4.2.2.2 Struts

The long strut must be divided in three parts for the calculation. The first one is in the presence of a flat surface, which is the wheel, the second part is in clean air and the last one is in presence of a smaller strut.

$$\frac{D_{s1}}{qS} = \sum C_{Ds} \frac{l_s d_s}{S} R_1 R_2 R_3 = C_{Ds} \frac{d_s}{S} \sum l_s R_2 R_3$$

$$\begin{aligned} \frac{D_{s1}}{qS} &= 1.2 \times \frac{0.11}{25.08} \times (0.345 \times 1 \times 1.15 + 0.589 \times 1 \times 1 + 0.16 \times 1.14 \times 1.1) \\ &= 6.24 \times 10^{-3} \end{aligned}$$

For the second strut, with 50 mm of diameter:

$$\frac{D_{s2}}{qS} = C_{Ds} \frac{l_s d_s}{qS} R_1 R_2 R_3 = 1.2 \times \frac{0.36 \times 0.05}{25.08} \times 1 \times 0.92 \times 1.05 = 0.83 \times 10^{-3}$$

The drag of the smallest strut, which connects the main strut and the door, is calculated as a cylinder in free flow.

$$\frac{D_{s3}}{qS} = C_{Ds} \frac{l_s d_s}{qS} = 1.2 \times \frac{0.18 \times 0.02}{25.08} = 0.17 \times 10^{-3}$$

So, the whole system of struts:

$$\frac{D_s}{qS} = \frac{D_{s1}}{qS} + \frac{D_{s2}}{qS} + \frac{D_{s3}}{qS} = (6.24 + 0.83 + 0.17) \times 10^{-3} = 7.24 \times 10^{-3}$$

4.2.2.3 Door

Following the same procedure as the lateral doors of the front gear:

$$\frac{D_d}{qS} = C_{Dd} \frac{t_d w_d}{S} + C_{Fd} \frac{S_{wet}}{S} = 1 \times \frac{0.01 \times 1.1}{25.08} + 0.0035 \times \frac{2 \times 0.4}{25.08} = 0.55 \times 10^{-3}$$

4.2.2.4 Cavity

The drag of the cavity is function of the exposed area, which can be obtained from CATIA.

$$\frac{D_c}{qS} = C_{Dc} \frac{S_{exposed}}{S} = 0.021 \times \frac{0.9}{25.08} = 0.75 \times 10^{-3}$$

Knowing that the effect due to the thickness of the wing, F_1 , is given in the Figure 8 of the ESDU document [17], the total drag coefficient can be calculated,

$$\begin{aligned} \frac{D_{main}}{qS} &= 2 \left[\frac{D_w}{qS} + \frac{D_s}{qS} + \frac{D_d}{qS} + \frac{D_c}{qS} \right] F_1 = 2 \times (1.68 + 7.24 + 0.55 + 0.75) \times 1.2 \times 10^{-3} \\ &= 0.0245 \end{aligned}$$

MAIN GEAR DRAG

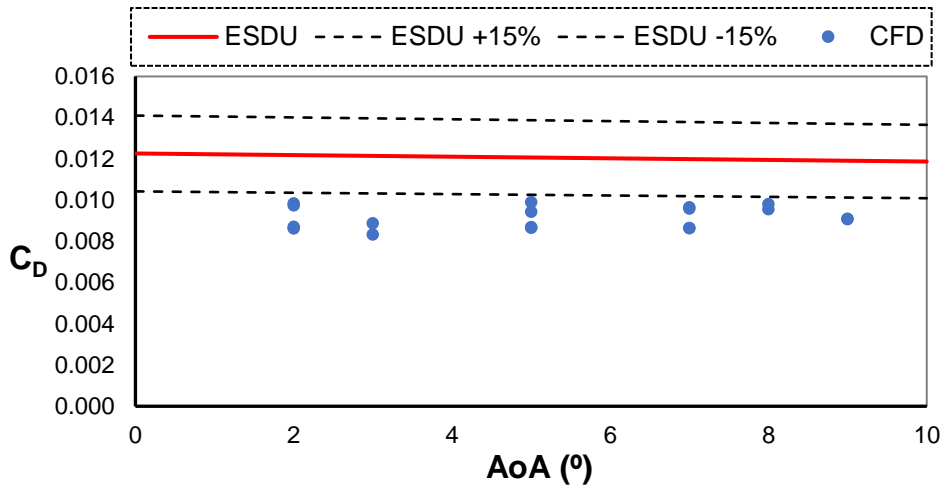


Figure 4.2.6. Drag coefficient of each main gear mechanism

Figure 4.2.6 shows the drag coefficients of each mechanism that forms the main gear calculated with empirical methods and CFD. The conclusions reached analysing the front gear drag are valid for the main gear too. The drag of the main gear is also underestimated, and it is independent of the angle of attack because it is constant for the cases studied.

The same effect as the reduction in the angle of attack of the front gear can be seen in the Figure 4.2.7, but in this case the flow around the main gear is influenced by the presence of the wing.

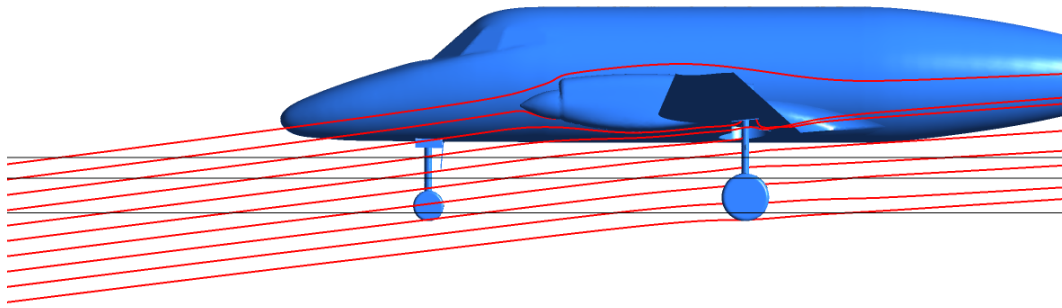


Figure 4.2.7. Flow past the main gear, $M=0.25$ $\alpha=7^\circ$. (Horizontal lines plotted to visualize the change in angle of the streamlines)

Therefore, the total drag of the undercarriage is:

$$\frac{D_{Tot}}{qS} = \frac{D_{Front}}{qS} + \frac{D_{Main}}{qS} = 0.0115 + 0.0245 = 0.036$$

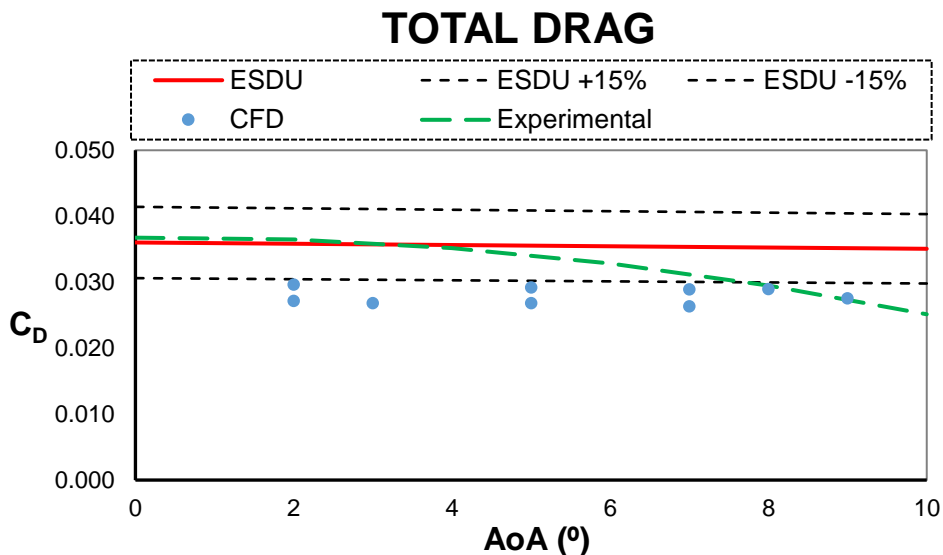


Figure 4.2.8. Total drag, comparison of different methods

Figure 4.2.8 shows the total drag estimated with empirical methods and CFD, as the previous figures, but in this case, the drag increment measured in the experiments is added. The green line represents the difference between the experiments at UCDWN configuration and cruise, giving the total drag of the landing gear. This line was calculated numerically subtracting fit line of the drag at CR configuration presented in section 4.1 to the drag at UCDWN configuration for every angle of attack. Comparing this line with the other methods, the conclusions would be:

- ESDU predicts the drag very accurately for $\alpha=0^\circ$, which was the assumption made to calculate the drag with this technique.
- The difference between ESDU and the experimental data increases with the angle of attack. The errors start becoming significant (5%) from $\alpha=5^\circ$.
- CFD underpredicts the drag coefficient. If more details were included in the undercarriage the drag of the model would increase.

5 CONCLUSIONS AND FURTHER RECOMMENDATIONS

5.1 Conclusions

The undercarriage drag of the BAE Jetstream 31 has been studied by a CFD analysis and compared to those obtained from the flight experiments and empirical methods, in this case ESDU 79015 [17]. While the empirical methods consider the drag of each component separately and then sum all of them, the flight experiments carried out can estimate the drag change for different configurations. This limitation of the flight experiments has led to a comparison of the total drag estimates instead of component drag coefficients.

The results have shown that CFD underpredicts the total drag of the landing gear always falling just below the prediction intervals of the ESDU, being the values obtained around 20% lower than ESDU. Previous studies [19] have shown that the empirical estimates are closer to the CFD when the landing gear is considered in free air so the influence of the whole aircraft in the undercarriage drag is considerable.

Decomposing the total drag in each gear, the drag of the front gear is 15% lower than ESDU while the main gear drag is around 25% lower, which shows that the biggest error comes from the main gear. This difference should be checked again when the propellers are added to the model as the main gear is located directly in the slipstream of the blades.

Further comparison of the empirical, experimental and CFD results have shown that the error of ESDU varies from an underprediction of 2% at 0° AoA up to an overprediction of 40% at 10° AoA, due to reduction in drag from the experimental data. However, the total drag of the landing gear falls within the prediction intervals of the ESDU from 0° to 6° AoA.

Meanwhile, comparing the results obtained from CFD with the experimental data using the lift and drag curves, the computational model is just below the experimental data. However, the slopes of the lift and drag curves are predicted very closely. The error begins to increase at high angles of attacks where the

difference in the onset of separation between the model and the experiments becomes relevant. This should be improved with the addition of the propellers to the model as can be seen in previous studies for CR configuration.

Finally, the reach has shown that the biggest contributors to the drag are the struts, wheels and the back door of the front gear, while the front gear cavity and lateral door drag is almost negligible. Therefore, if a reduction in drag is wanted the most effective way to achieve such goal is to give a more aerodynamic shape to the struts and door. A common solution for fixed landing gears is to use fairings in the wheels but in the case considered, a retractable landing gear, these are not used. The main gear cavity drag can also be reduced using rounded edges or wider edges to reduce the severity of the backward facing step.

5.2 Future work

Having discussed the results and based on the modifications made to the computational model, the following work is proposed for a better understanding of the flowfield and discrepancies between the model and the experimental data:

- Following the same steps as previous years with the CR model, the addition of the propellers using user defined functions is necessary to analyse their effect, particularly at high angles of attack and the interaction with the undercarriage.
- The literature review has shown that a study of the aeroacoustics of the landing gear could be interesting because many of the latest publications related to landing gears are focusing their studies in this area.

6 REFERENCES

- [1] *National Flying Laboratory Centre* (no date a).
- [2] Raymer, D. P. (2012) *Aircraft Design: A Conceptual Approach*. Fifth Edit. Edited by J. A. Schetz. Reston, Virginia: American Institute of Aeronautics and Astronautics.
- [3] Anderson, J. D. (2001) *Fundamentals of Aerodynamics*. 3rd editio. Singapore: McGraw-Hill.
- [4] IHS ESDU (1986) 'ESDU 80025. Mean forces, pressures and flow field velocities for circular cylindrical structures: single cylinder with two-dimensional flow.', (October 1980).
- [5] Schlichting, H. (2014) 'Boundary Layer Theory', *Aircraft Engineering and Aerospace Technology*. doi: 10.1108/eb029898.
- [6] Gillis, T., Marichal, Y., Winckelmans, G. and Chatelain, P. (2019) 'A 2D immersed interface Vortex Particle-Mesh method', *Journal of Computational Physics*. Elsevier Inc., 394, pp. 700–718. doi: 10.1016/j.jcp.2019.05.033.
- [7] Abrahamsen Prsic, M., Ong, M. C., Pettersen, B. and Myrhaug, D. (2019) 'Large Eddy simulations of flow around tandem circular cylinders in the vicinity of a plane wall', *Journal of Marine Science and Technology*, 24(2), pp. 338–358. doi: 10.1007/s00773-018-0553-3.
- [8] Chen, X. and Xia, H. (2019) 'Flow and surface heat transfer analysis of a square cylinder in turbulent cross-flow', *Numerical Heat Transfer, Part A: Applications*. Taylor & Francis, 75(12), pp. 795–823. doi: 10.1080/10407782.2019.1594337.
- [9] Liang, H. and Duan, R.-Q. (2019) 'Effect of Lateral End Plates on Flow Crossing a Yawed Circular Cylinder', *Applied Sciences*, 9(8). doi: 10.3390/app9081590.
- [10] Royal, T. and Society, A. (2009) 'Aerodynamics and aero-acoustics of rectangular planform cavities. Part IIIA: Alleviation of unsteady flow effects – Introduction', (June).
- [11] Choi, H. H., Nguyen, V. T. and Nguyen, J. (2016) 'Numerical Investigation of Backward Facing Step Flow over Various Step Angles', *Procedia Engineering*. The Author(s), 154(1983), pp. 420–425. doi: 10.1016/j.proeng.2016.07.508.
- [12] Armaly, B. and Durst, F. (1983) 'Experimental and theoretical investigation of backward-facing step flow', *Journal of Fluid Mechanics*, 127. Available at: http://journals.cambridge.org/abstract_S0022112083002839.
- [13] Chen, L., Asai, K., Nonomura, T., Xi, G. and Liu, T. (2018) 'A review of Backward-Facing Step (BFS) flow mechanisms, heat transfer and control', *Thermal Science and Engineering Progress*. Elsevier, 6(January), pp. 194–216. doi: 10.1016/j.tsep.2018.04.004.
- [14] Xu, F., Gao, Z., Ming, X., Xia, L., Wang, Y., Sun, W. and Ma, R. (2015) 'The optimization for the backward-facing step flow control with synthetic jet based on experiment', *Experimental Thermal and Fluid Science*. Elsevier Inc., 64, pp. 94–107. doi: 10.1016/j.expthermflusci.2015.02.014.
- [15] Savory, E., Toy, N., Disimile, P. J. and Dimicco, R. G. (1993) 'The drag of three-dimensional rectangular cavities', *Applied Scientific Research*, 50(3–4), pp. 325–346. doi: 10.1007/BF00850565.
- [16] Shiyani, D. and Disimile, P. (2017) 'Effect of Yaw Angle on Drag Over Clean Rectangular

Cavities’.

[17] The Royal Aeronautical Society (1987) *ESDU 79015: Undercarriage drag prediction methods*. The Royal Aeronautical Society.

[18] Sese, C. (2013) *3D CFD Modelling of the Undercarriage and Propeller Effects on the Scottish Aviation Bulldog*. Cranfield University.

[19] Bennett, C. J., Lawson, N. and Gautrey, J. (2017) ‘Undercarriage drag prediction for a fixed undercarriage light aircraft’, in *AIAA AVIATION Forum* (ed.). Denver, Colorado, USA, 5-9 June 2017: AIAA 2017-4464. doi: 10.2514/6.2017-4464.

[20] Hedges, L. S., Travin, A. K. and Spalart, P. R. (2002) ‘Detached-Eddy Simulations Over a Simplified Landing Gear’, *Journal of Fluids Engineering*, 124(2), pp. 413–423. doi: 10.1115/1.1471532.

[21] Sadrehaghighi, I. (2019) ‘Mesh Generation in CFD’. doi: 10.13140/RG.2.2.26522.54721/2.

[22] Iaccarino, G., Ooi, A., Durbin, P. A. and Behnia, M. (2003) ‘Reynolds averaged simulation of unsteady separated flow’, *International Journal of Heat and Fluid Flow*, 24(2), pp. 147–156. doi: 10.1016/S0142-727X(02)00210-2.

[23] Wauters, J., Degroote, J. and Vierendeels, J. (2019) ‘Comparative Study of Transition Models for High-Angle-of-Attack Behavior’, *AIAA Journal*, pp. 1–16. doi: 10.2514/1.J057249.

[24] Parker, R. (2006) *Investigation and Development of a 3D Non-Contact Scanning Process for CFD Model Generation*. Cranfield University.

[25] Vessot, C. (2012) *CFD Aerodynamic Model of the Jetstream 31*. Cranfield University.

[26] Lawson, N. J., Jacques, H., Gautrey, J. E., Cooke, A. K., Holt, J. C. and Garry, K. P. (2017) ‘Jetstream 31 national flying laboratory: Lift and drag measurement and modelling’, *Aerospace Science and Technology*. Elsevier Masson SAS, 60, pp. 84–95. doi: 10.1016/j.ast.2016.11.001.

[27] Le Pajolec, M. (2013) *Investigation of Propeller theories on BAE Jetstream 31 CFD Model*. Cranfield University.

[28] Jacques, H. (2014) *Simulation of propeller effects on the jetstream 31 aircraft*. Cranfield University.

[29] K.A, A. F. (2016) *CFD ANALYSIS OF PROPELLER EFFECTS ON JETSTREAM - 31*. Cranfield University.

[30] Jacques, H. (2014) *Simulation of Propeller Effects on the Jetstream 31 Aircraft*. Cranfield University.

[31] Ricciardi, T. R., Wolf, W. R. and Speth, R. (2018) ‘Acoustic Prediction of LAGOON Landing Gear: Cavity Noise and Coherent Structures’, *AIAA Journal*, 56(11), pp. 4379–4399. doi: 10.2514/1.j056957.

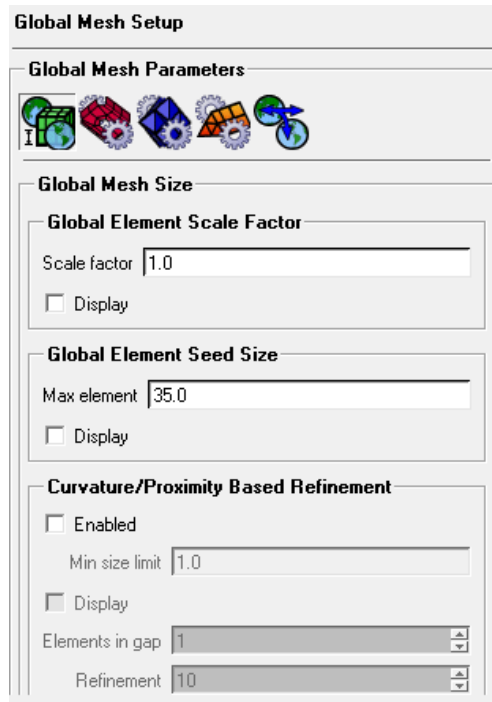
[32] Imamura, T., Hirai, T., Amemiya, K., Yokokawa, Y., Enomoto, S. and Yamamoto, K. (2010) ‘Reprint of: Aerodynamic and aeroacoustic simulations of a two-wheel landing gear’, *Procedia IUTAM*. Elsevier, 1(2009), pp. 293–302. doi: 10.1016/j.piutam.2010.10.031.

[33] Lockard, D., Khorrami, M. and Li, F. (2012) ‘High Resolution Calculation of a Simplified Landing Gear’, pp. 1–11. doi: 10.2514/6.2004-2887.

[34] Bennett, G. J., Neri, E. and Kennedy, J. (2018) 'Noise Characterization of a Full-Scale Nose Landing Gear', *Journal of Aircraft*, 55(6), pp. 2476–2490. doi: 10.2514/1.c034750.

Appendix A. PARAMETERS OF THE MESH

The following figures show the parameters defined to generate the mesh chosen after the mesh sensitivity analysis. Note that all the values are in meters.



Global Mesh Setup

Global Mesh Parameters

Global Mesh Size

Global Element Scale Factor

Scale factor: 1.0

Display

Global Element Seed Size

Max element: 35.0

Display

Curvature/Proximity Based Refinement

Enabled

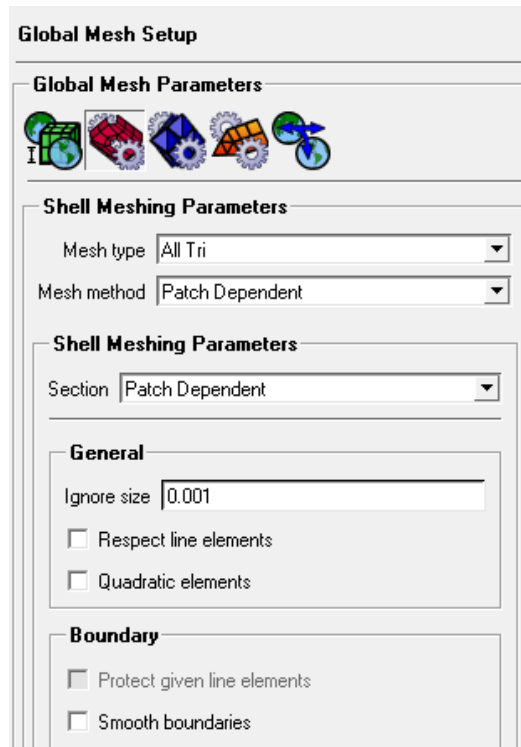
Min size limit: 1.0

Display

Elements in gap: 1

Refinement: 10

Appendix A. Figure 1. Global mesh setup. Global mesh size.



Global Mesh Setup

Global Mesh Parameters

Shell Meshing Parameters

Mesh type: All Tri

Mesh method: Patch Dependent

Shell Meshing Parameters

Section: Patch Dependent

General

Ignore size: 0.001

Respect line elements

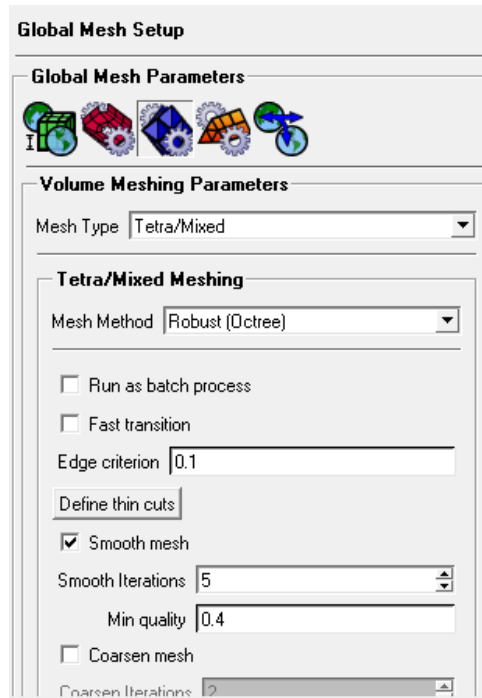
Quadratic elements

Boundary

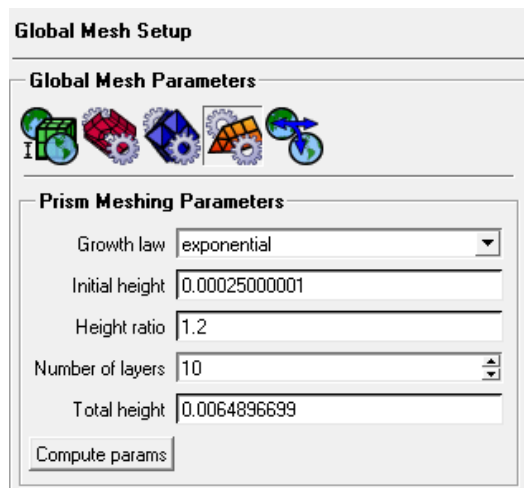
Protect given line elements

Smooth boundaries

Appendix A. Figure 2. Global mesh setup. Shell meshing parameters.



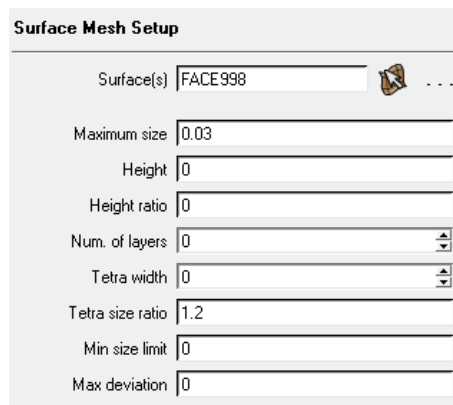
Appendix A. Figure 3. Global mesh setup. Volume meshing parameters.



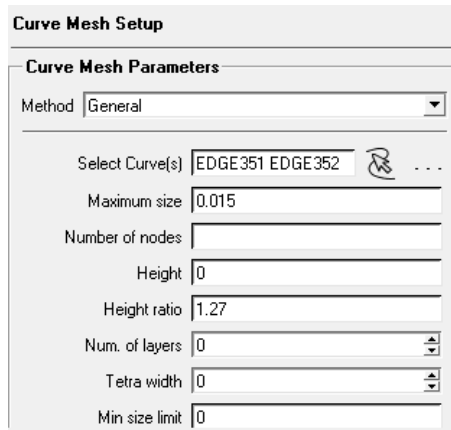
Appendix A. Figure 4. Global mesh setup. Prism meshing parameters.

Part ▲	Prism	Hexa-core	Maximum size
AXIS			
FARFIELD	<input type="checkbox"/>		35
FLUID	<input type="checkbox"/>	<input checked="" type="checkbox"/>	
FRONT_GEAR/BACK_DOOR	<input checked="" type="checkbox"/>		
FRONT_GEAR/CAVITY	<input checked="" type="checkbox"/>		0.03
FRONT_GEAR/DOOR1	<input checked="" type="checkbox"/>		
FRONT_GEAR/DOOR2	<input checked="" type="checkbox"/>		
FRONT_GEAR/STRUT	<input checked="" type="checkbox"/>		0.03
FRONT_GEAR/WHEEL1	<input checked="" type="checkbox"/>		
FRONT_GEAR/WHEEL2	<input checked="" type="checkbox"/>		
FUSELAGE	<input checked="" type="checkbox"/>		
GEOM			
H_ESTABILIZER/PORT/AREA	<input checked="" type="checkbox"/>		0.15
H_ESTABILIZER/PORT/LOWER	<input checked="" type="checkbox"/>		0.15
H_ESTABILIZER/PORT/TIP	<input checked="" type="checkbox"/>		0.15
H_ESTABILIZER/PORT/UPPER	<input checked="" type="checkbox"/>		0.15
H_ESTABILIZER/STBD/AREA	<input checked="" type="checkbox"/>		0.15
H_ESTABILIZER/STBD/LOWER	<input checked="" type="checkbox"/>		0.15
H_ESTABILIZER/STBD/TIP	<input checked="" type="checkbox"/>		0.15
H_ESTABILIZER/STBD/UPPER	<input checked="" type="checkbox"/>		0.15
INLET	<input type="checkbox"/>		35
LOWER_TAIL	<input checked="" type="checkbox"/>		0.15
MAIN_GEAR/PORT/CAVITY	<input checked="" type="checkbox"/>		0.03
MAIN_GEAR/PORT/DOOR	<input checked="" type="checkbox"/>		0.03
MAIN_GEAR/PORT/STRUT	<input checked="" type="checkbox"/>		0.03
MAIN_GEAR/PORT/WHEEL	<input checked="" type="checkbox"/>		
MAIN_GEAR/STBD/CAVITY	<input checked="" type="checkbox"/>		0.03
MAIN_GEAR/STBD/DOOR	<input checked="" type="checkbox"/>		0.03
MAIN_GEAR/STBD/STRUT	<input checked="" type="checkbox"/>		0.03
MAIN_GEAR/STBD/WHEEL	<input checked="" type="checkbox"/>		
OUTLET	<input type="checkbox"/>		35
V_ESTABILIZER/PORT	<input checked="" type="checkbox"/>		0.15
V_ESTABILIZER/STBD	<input checked="" type="checkbox"/>		0.15
V_ESTABILIZER/TIP	<input checked="" type="checkbox"/>		0.15
WINGS/PORT/ENGINE	<input checked="" type="checkbox"/>		0.15
WINGS/PORT/JOIN	<input checked="" type="checkbox"/>		0.15
WINGS/PORT/LOWER	<input checked="" type="checkbox"/>		0.15
WINGS/PORT/TIP	<input checked="" type="checkbox"/>		0.15
WINGS/PORT/UPPER	<input checked="" type="checkbox"/>		0.15
WINGS/STBD/ENGINE	<input checked="" type="checkbox"/>		0.15
WINGS/STBD/JOIN	<input checked="" type="checkbox"/>		0.15
WINGS/STBD/LOWER	<input checked="" type="checkbox"/>		0.15
WINGS/STBD/TIP	<input checked="" type="checkbox"/>		0.15
WINGS/STBD/UPPER	<input checked="" type="checkbox"/>		0.15

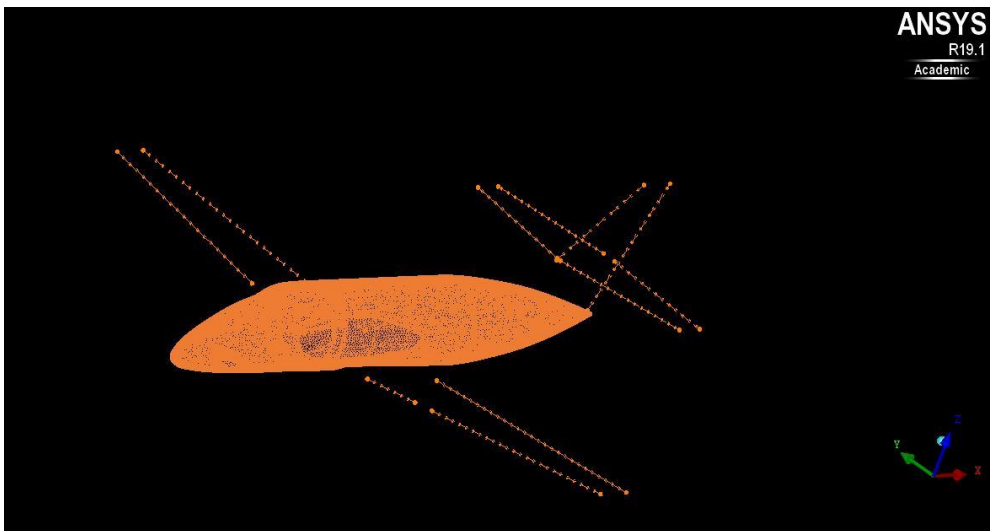
Appendix A. Figure 5. Part mesh setup. (The highlighted part were defined using surface and curve mesh tools)



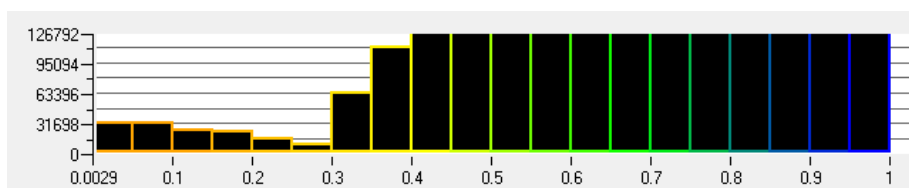
Appendix A. Figure 6. Surface mesh setup.



Appendix A. Figure 7. Curve mesh setup. (The number of nodes is different for each line, depending on the length and cell size)



Appendix A. Figure 8. Location of mesh densities relative to the fuselage to capture the flow around the leading and trailing edges.



Appendix A. Figure 9. Mesh quality histogram. (The worst cells are located near the sharp edges as the edge of the cavity and trailing edge)

Appendix B. FLUENT SETTINGS

These are the settings used for the simulations in fluent.

General

Mesh

Scale... Check Report Quality

Display...

Solver

Type _____ Velocity Formulation

Pressure-Based Absolute

Density-Based Relative

Time _____

Steady

Transient

Appendix B. Figure 1. General settings

Models

Models

Multiphase - Off

Energy - On

Viscous - SST k-omega

Radiation - Off

Heat Exchanger - Off

Species - Off

Discrete Phase - Off

Acoustics - Off

Electric Potential - Off

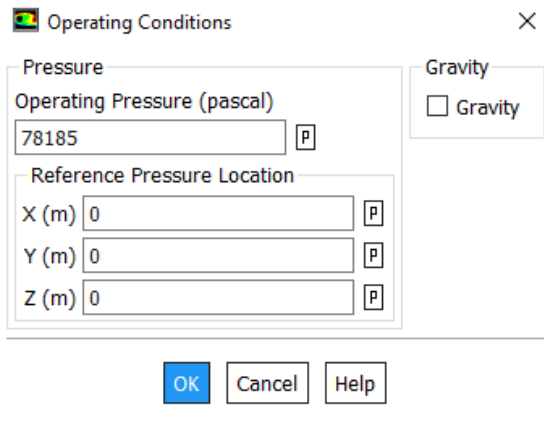
Appendix B. Figure 2. Models

Name	air	Material Type	fluid
Chemical Formula		Fluent Fluid Materials	air
		Mixture	none

Properties

Density (kg/m ³)	ideal-gas	Edit...
Cp (Specific Heat) (j/kg-k)	constant	Edit...
	1006.43	
Thermal Conductivity (w/m-k)	constant	Edit...
	0.0242	
Viscosity (kg/m-s)	sutherland	Edit...
Molecular Weight (kg/kmol)	constant	Edit...
	28.966	

Appendix B. Figure 3. Fluid properties



Operating Conditions

Pressure

Operating Pressure (pascal)

78185 P

Reference Pressure Location

X (m) 0 P

Y (m) 0 P

Z (m) 0 P

Gravity

Gravity

OK Cancel Help

Appendix B. Figure 4. Operating conditions

Pressure Far-Field ×

Zone Name
farfield

Momentum Thermal Radiation Species Potential UDS DPM

Gauge Pressure (pascal) 0 constant

Mach Number 0.2 constant

Coordinate System Cartesian (X, Y, Z)

X-Component of Flow Direction 0.9986 constant

Y-Component of Flow Direction 0 constant

Z-Component of Flow Direction 0.0523 constant

Turbulence
Specification Method Intensity and Viscosity Ratio

Turbulent Intensity (%) 5

Turbulent Viscosity Ratio 10

Momentum Thermal Radiation Species Potential UDS DPM

Temperature (k) 280 constant

Appendix B. Figure 5. Farfield conditions ($M=0.2$, $\alpha=3^\circ$)

Reference Values

Compute from
farfield

Reference Values

Area (m2)	25.085
Density (kg/m3)	0.9728058
Enthalpy (j/kg)	284049.2
Length (m)	1.717
Pressure (pascal)	0
Temperature (k)	280
Velocity (m/s)	67.06371
Viscosity (kg/m-s)	1.7894e-05
Ratio of Specific Heats	1.4

Reference Zone
fluid

Appendix B. Figure 6. Reference values

Solution Methods

Formulation

Flux Type

Spatial Discretization

Gradient
<input type="text" value="Least Squares Cell Based"/>
Flow
<input type="text" value="Second Order Upwind"/>
Turbulent Kinetic Energy
<input type="text" value="First Order Upwind"/>
Specific Dissipation Rate
<input type="text" value="First Order Upwind"/>

Appendix B. Figure 7. Solution methods

Solution Controls

Courant Number

Under-Relaxation Factors

Turbulent Kinetic Energy
<input type="text" value="0.8"/>
Specific Dissipation Rate
<input type="text" value="0.8"/>
Turbulent Viscosity
<input type="text" value="1"/>
Solid
<input type="text" value="1"/>

Appendix B. Figure 8. Solution controls

Appendix C. DRAG COEFFICIENT OF EACH ELEMENT

These tables show the drag coefficients of each element from all the CFD simulations.

Mach number	Speed (knots)	alfa (deg)	Back door	Cavity	Lateral Doors		Strut	Wheels	
					1	2		1	2
0.18	117	8	37.55	7.93	1.09	1.14	19.38	14.47	14.46
0.2	130	9	41.29	5.37	0.91	1.01	15.51	14.44	15.33
		7	40.08	5.96	1.18	1.07	19.64	14.81	13.94
		5	41.94	5.38	1.22	1.11	19.95	14.23	14.72
		3	39.85	5.99	0.99	1.06	18.20	15.28	14.70
0.25	163	7	36.20	6.63	1.04	0.95	16.22	14.40	15.32
		5	40.50	5.36	1.09	0.96	16.74	15.62	14.53
		2	44.37	4.92	1.21	1.11	20.05	14.50	14.48
0.32	209	2	41.67	5.25	1.06	0.96	18.14	15.20	15.91

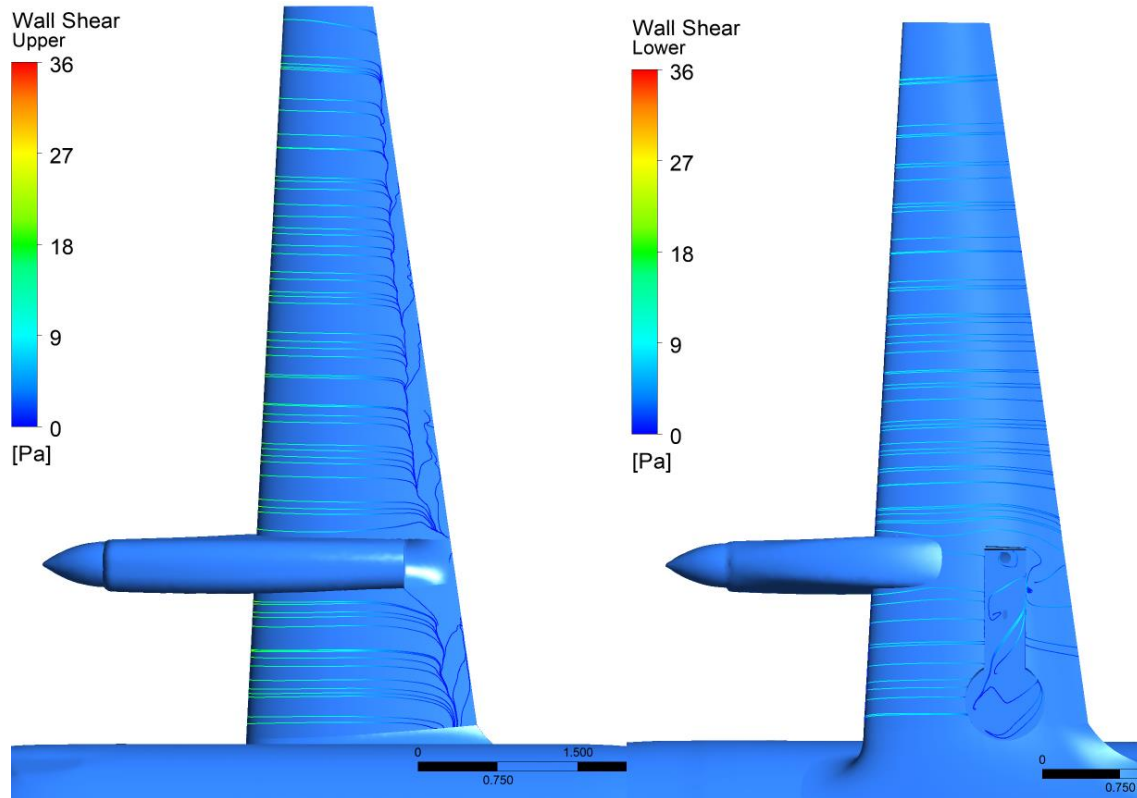
Appendix C. Table 1. The drag coefficient of each element in the front gear. (in drag counts)

Mach number	Speed (knots)	alfa (deg)	Port				Staboard			
			Cavity	Door	Strut	Wheel	Cavity	Door	Strut	Wheel
0.18	117	8	20.83	10.08	39.67	25.00	21.77	10.17	39.64	26.48
0.2	130	9	23.86	10.33	35.09	21.52	19.53	10.33	35.53	25.46
		7	21.88	9.88	39.92	24.76	19.88	9.86	38.72	27.43
		5	18.64	9.32	40.78	25.54	21.10	9.45	39.40	29.09
		3	20.57	8.93	30.88	22.93	19.04	8.70	34.17	26.82
0.25	163	7	20.26	9.67	32.97	23.46	21.51	9.91	30.94	24.01
		5	18.74	9.37	34.24	24.13	18.23	9.30	33.84	25.45
		2	19.89	8.90	42.07	27.55	19.68	8.96	41.06	27.70
0.32	209	2	19.00	8.65	34.31	24.30	18.20	8.53	35.13	25.09

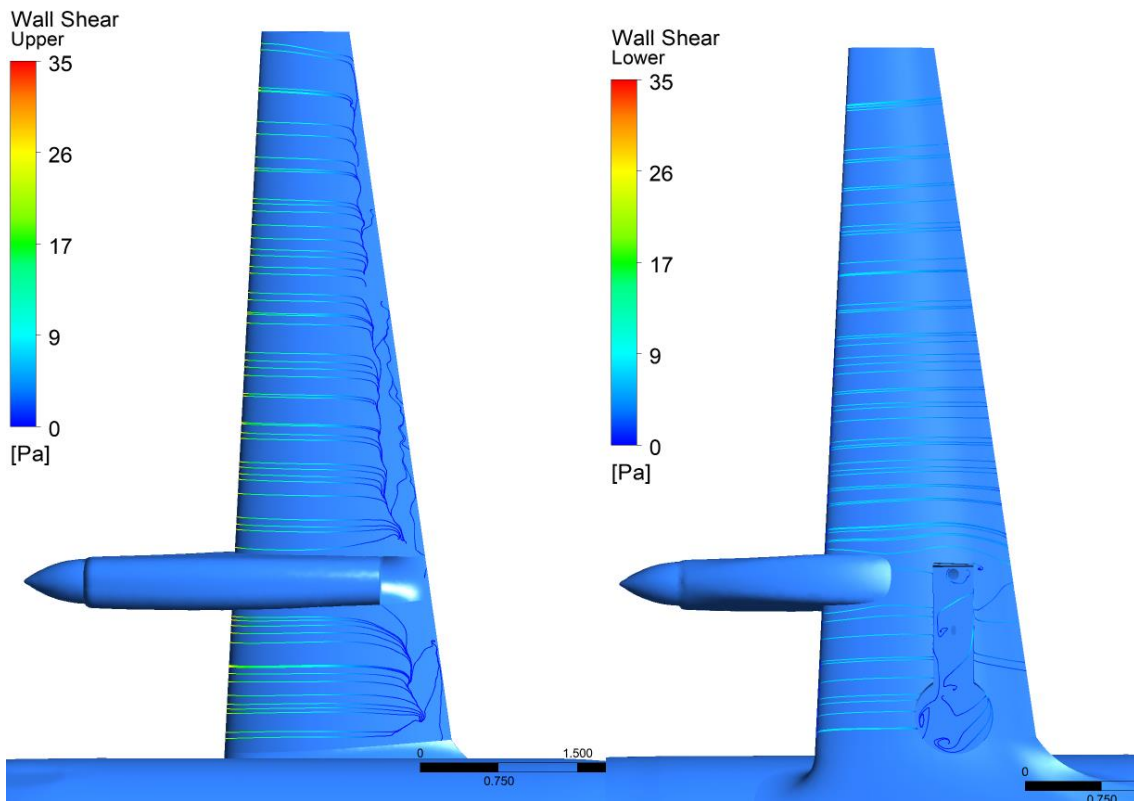
Appendix C. Table 2. The drag coefficient of each element in the main gear. (in drag counts)

Appendix D. FLOW VISUALIZATION

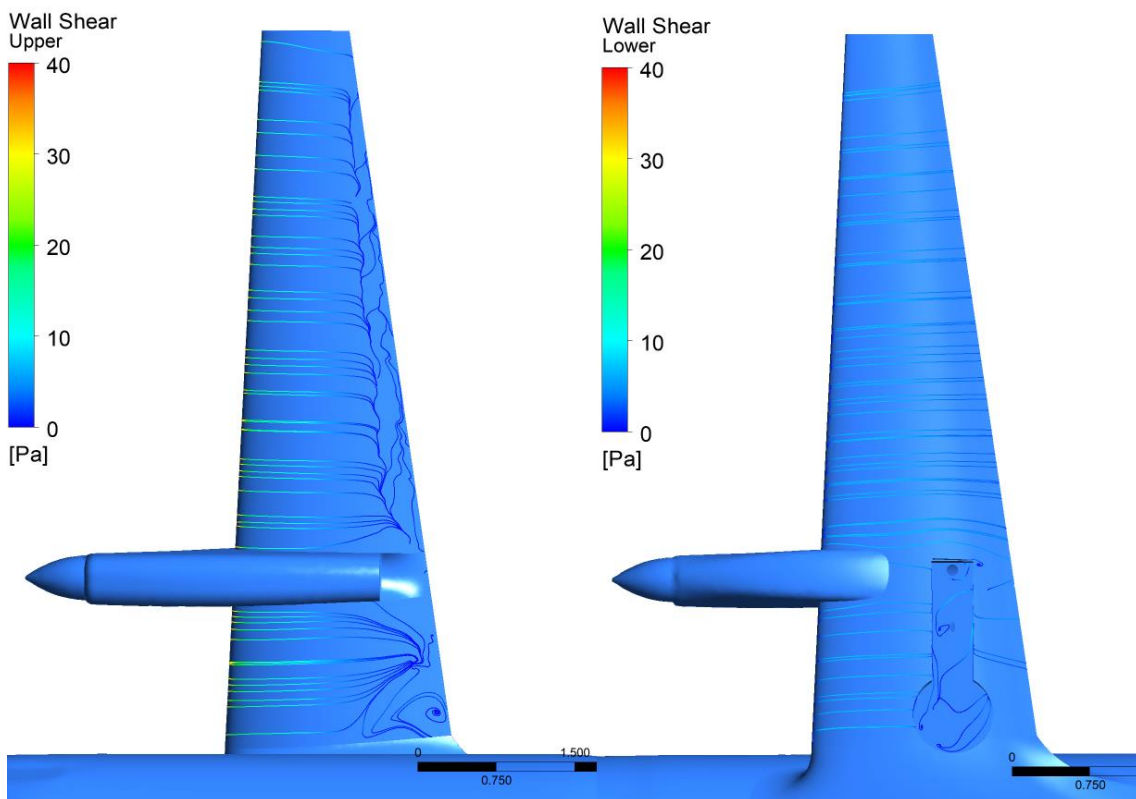
The figures show the surface flow visualization on the wings and under the fuselage where the flow is disturbed by the presence of the front landing gear. Note that the flow goes from left to right.



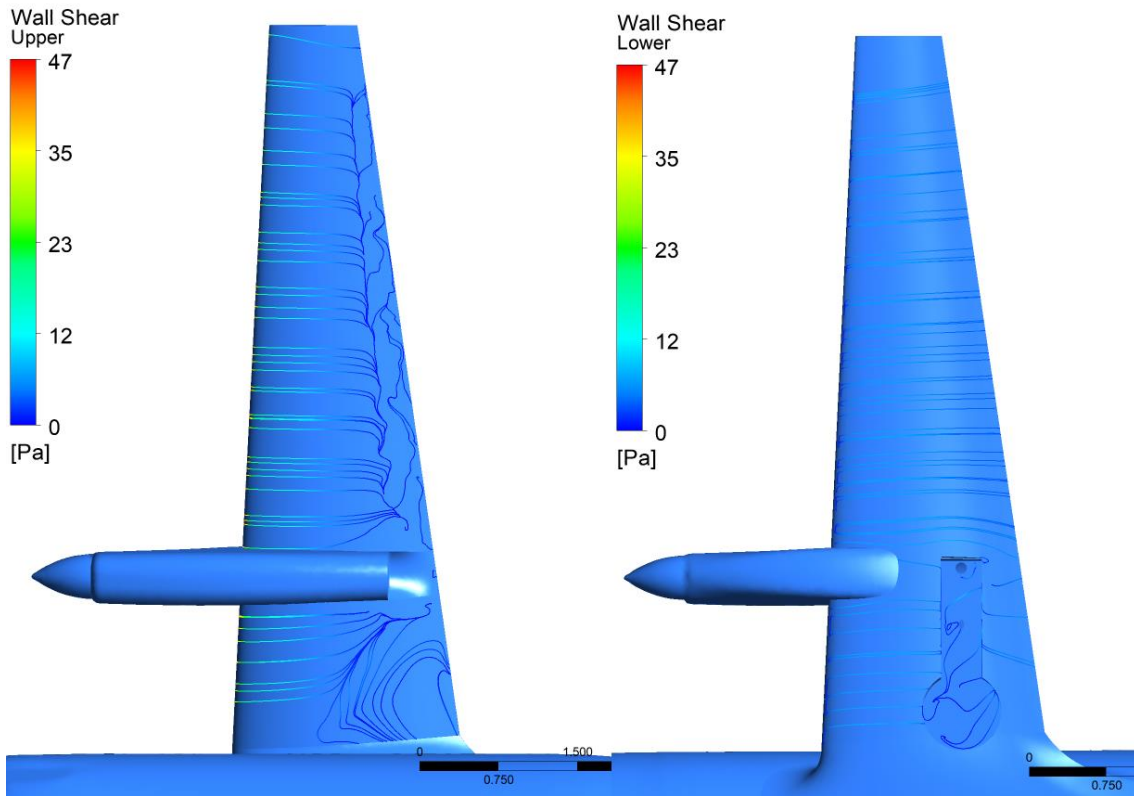
Appendix D. Figure 1. Flow visualization on the wing ($M=0.2$, $\alpha=3^\circ$)



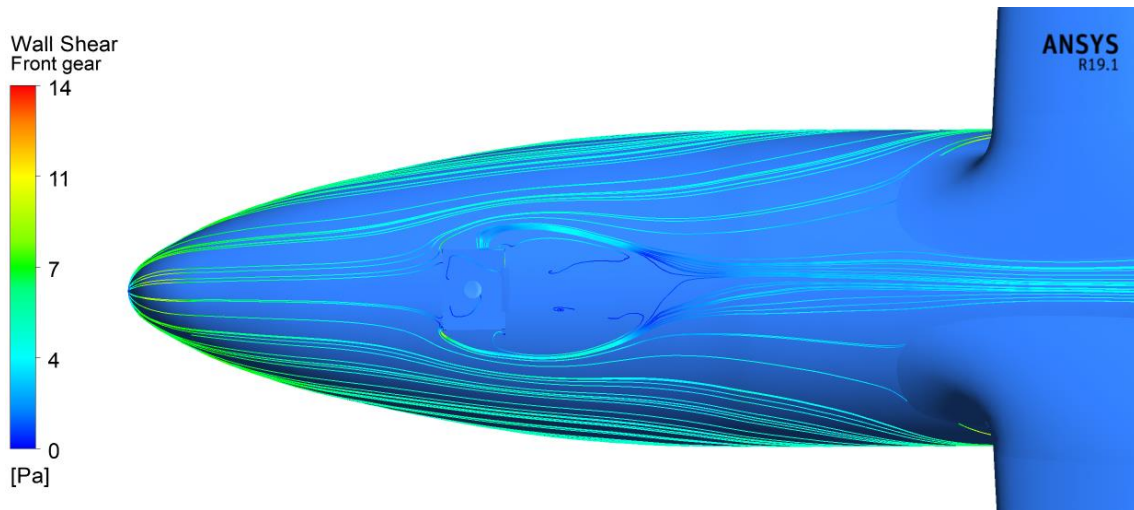
Appendix D. Figure 2. Flow visualization on the wing ($M=0.2$, $\alpha=5^\circ$)



Appendix D. Figure 3. Flow visualization on the wing ($M=0.2$, $\alpha=7^\circ$)



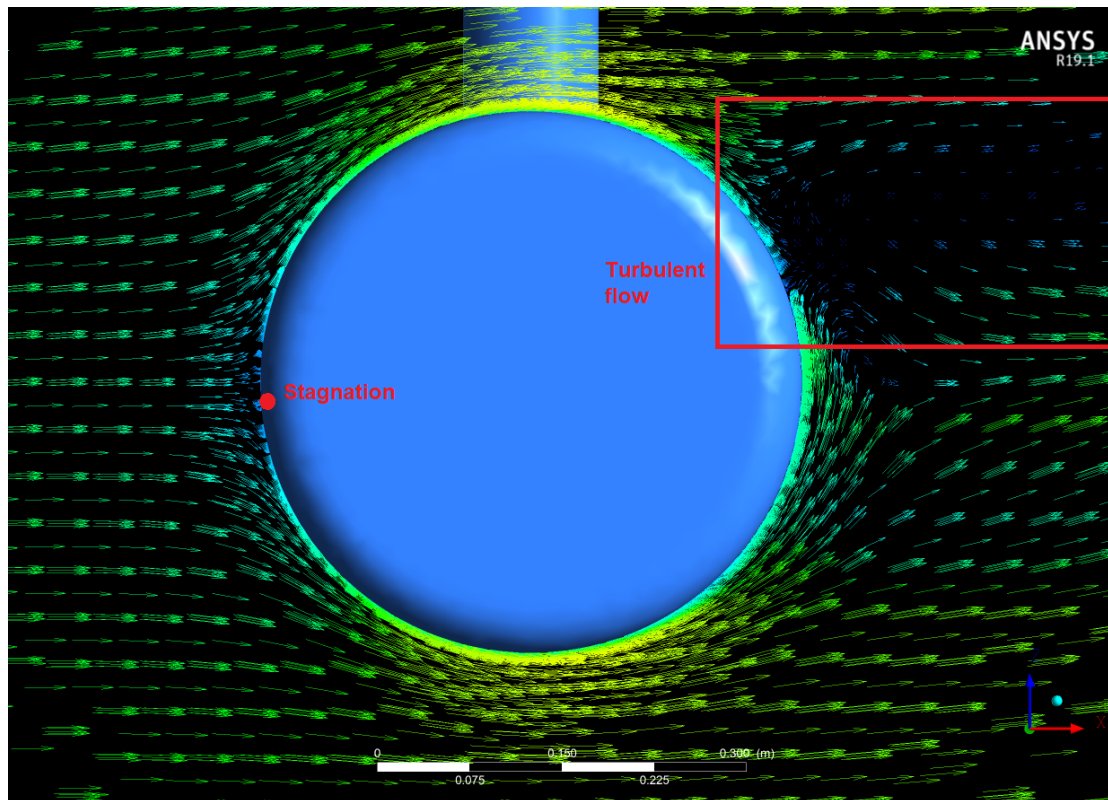
Appendix D. Figure 4. Flow visualization on the wing ($M=0.2$, $\alpha=9^\circ$)



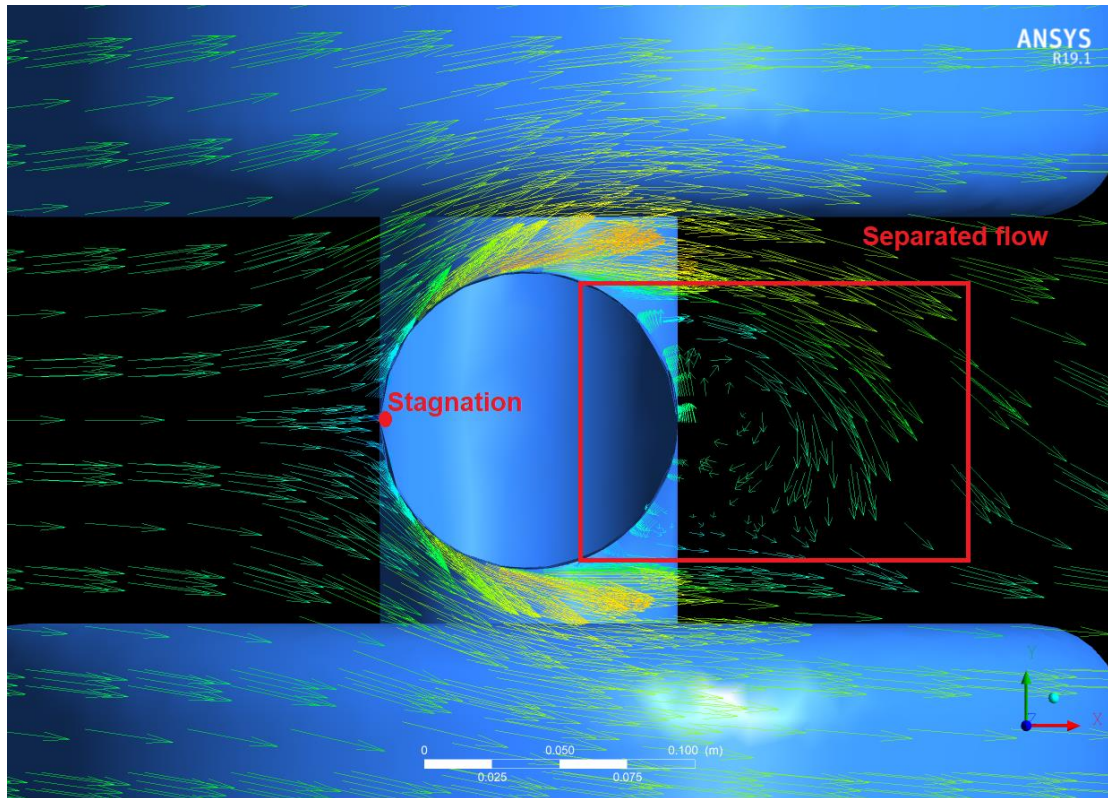
Appendix D. Figure 5. Flow visualization under the fuselage ($M=0.2$, $\alpha=5^\circ$)

Appendix E. FLOW STRUCTURE IN EACH COMPONENT

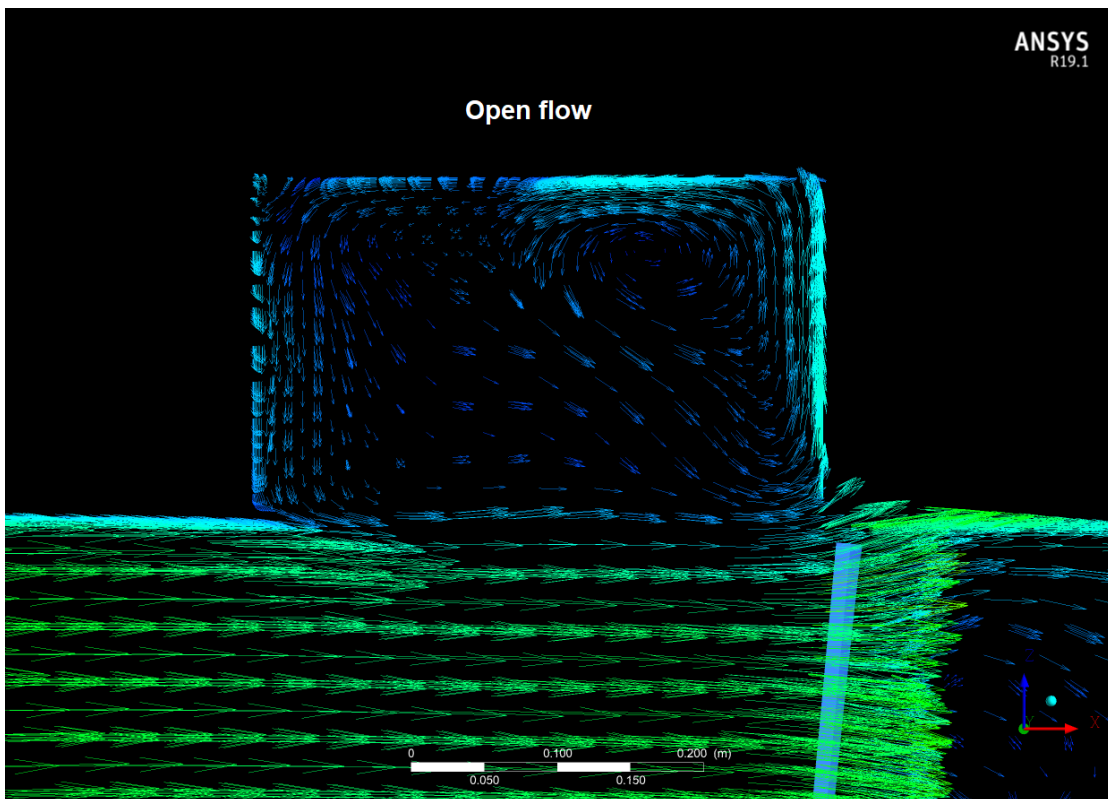
These figures show the 3D flow around every element of the landing gear, which can be used to compare the real flow with the 2D cases introduced in the literature review. Those were: the flow around a cylinder, a flat plate and cavities. The direction of the flow is from left to right.



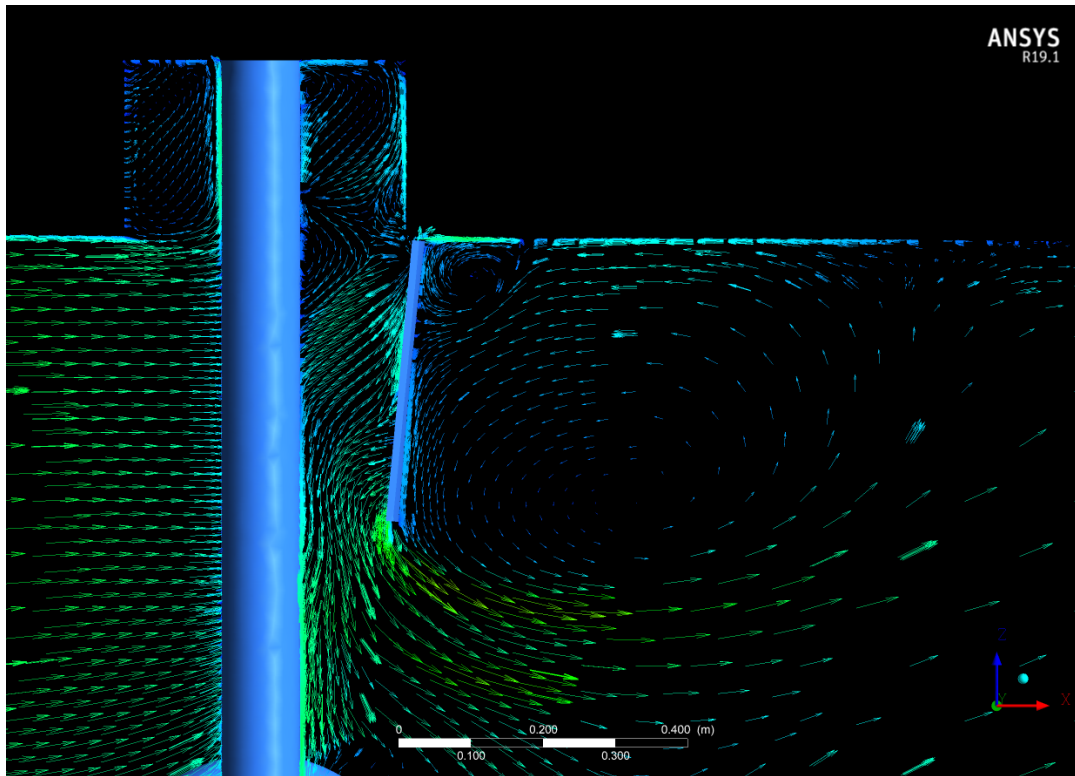
Appendix E. Figure 6. Flow around the front gear wheel. ($M=0.25$, $\alpha=2^\circ$)



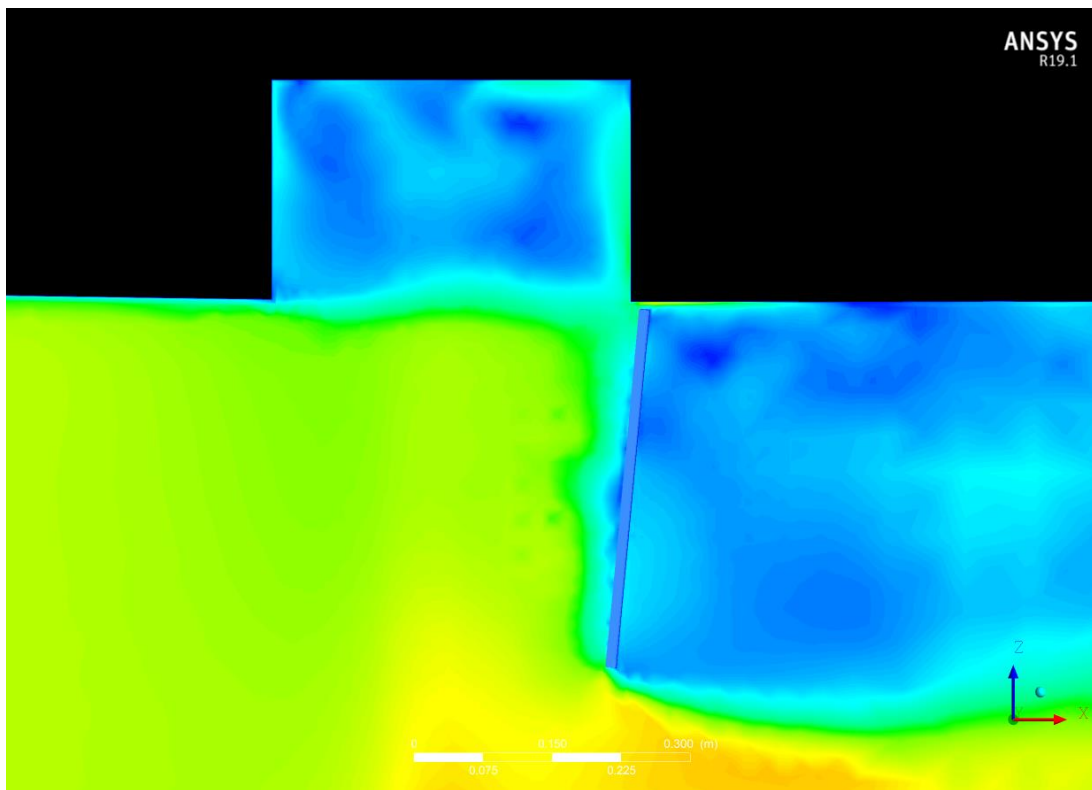
Appendix E. Figure 7. Flow around the front gear strut. ($M=0.25$, $\alpha=2^\circ$)



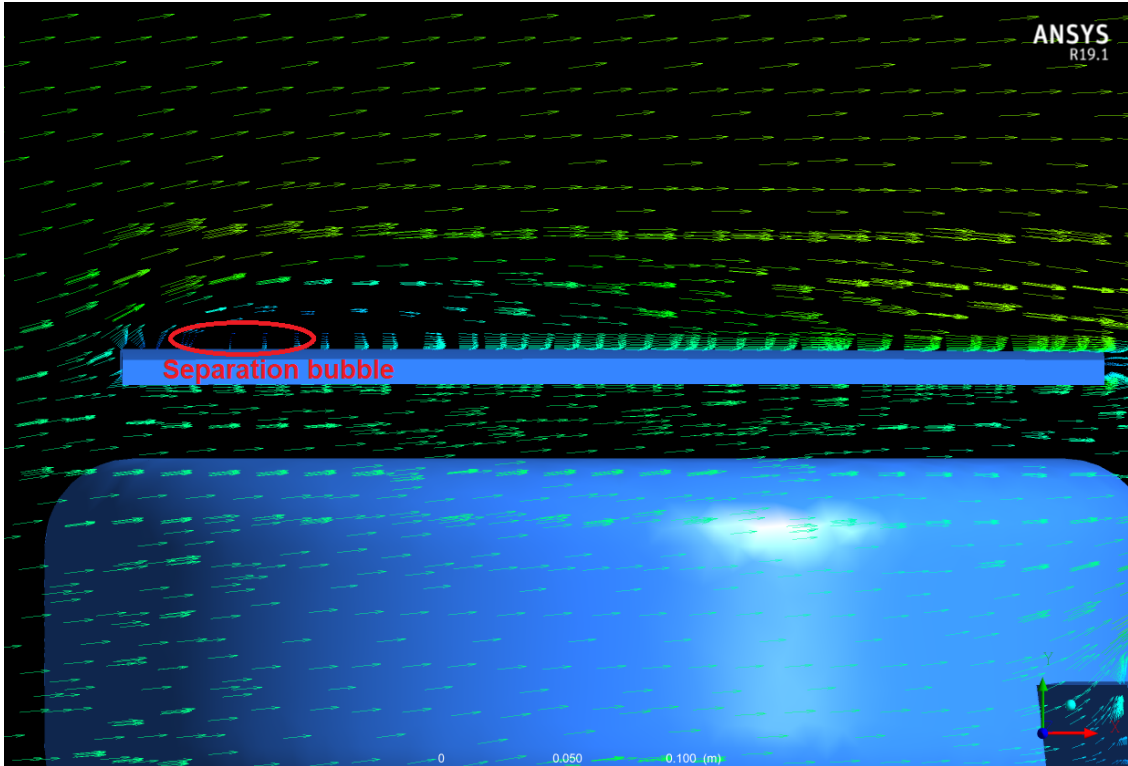
Appendix E. Figure 8. Flow inside the front gear open cavity. ($M=0.25$, $\alpha=2^\circ$, $Y=0.2\text{m}$)



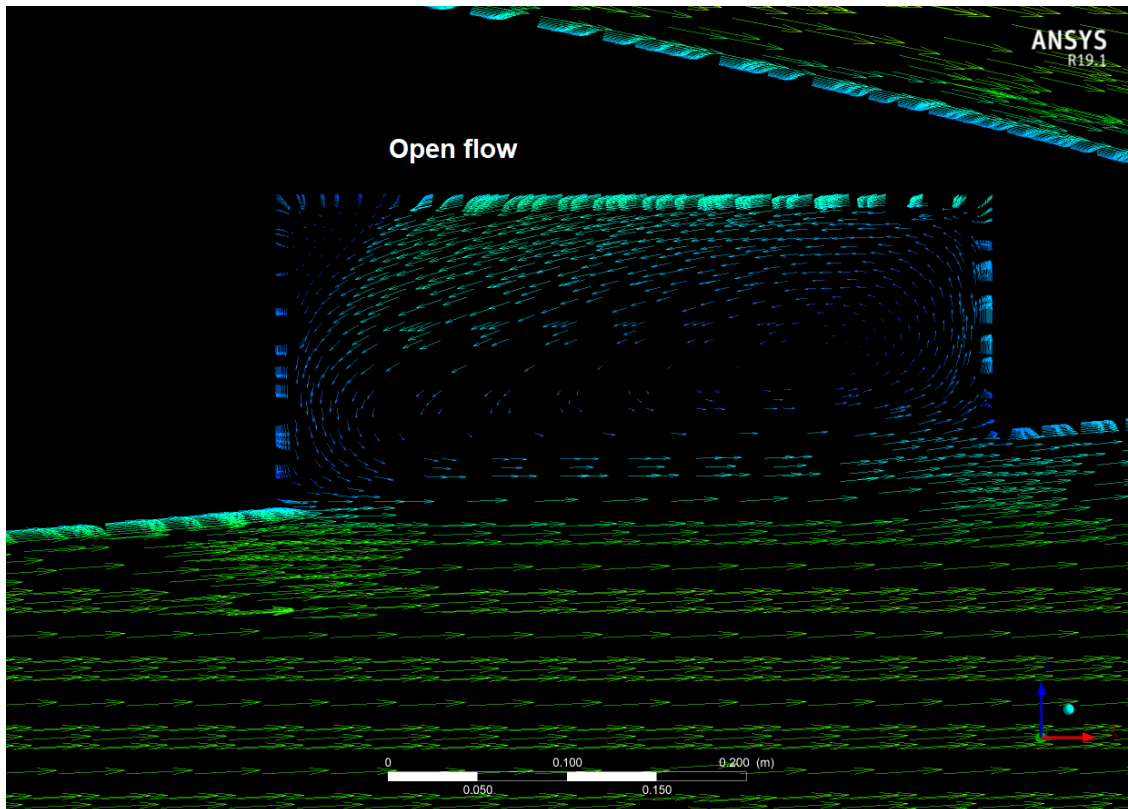
Appendix E. Figure 9. Recirculating flow behind the door perpendicular to the flow. ($M=0.25$, $\alpha=2^\circ$)



Appendix E. Figure 10. Pressure drop behind the door perpendicular to the flow. ($M=0.25$, $\alpha=2^\circ$, $Y=0.1\text{m}$)



Appendix E. Figure 11. Flow around the door parallel to the flow. ($M=0.25$, $\alpha=2^\circ$)



Appendix E. Figure 12. Main gear open cavity flow. ($M=0.25$, $\alpha=2^\circ$, $Y=2m$)